UCRL-JRNL-211920

LAWRENCE
LIVERMORE
NATIONAL
LABORATORY

Modeling aerosol-cloud interactions with a self-consistent cloud scheme in a general circulation model

Y. Ming, V. Ramaswamy, L. J. Donner, V. T. Phillips, S. A. Klein, P. A. Ginoux, L. H. Horowitz

May 3, 2005

Journal of Atmospheric Sciences

Disclaimer

This document was prepared as an account of work sponsored by an agency of the United States Government. Neither the United States Government nor the University of California nor any of their employees, makes any warranty, express or implied, or assumes any legal liability or responsibility for the accuracy, completeness, or usefulness of any information, apparatus, product, or process disclosed, or represents that its use would not infringe privately owned rights. Reference herein to any specific commercial product, process, or service by trade name, trademark, manufacturer, or otherwise, does not necessarily constitute or imply its endorsement, recommendation, or favoring by the United States Government or the University of California. The views and opinions of authors expressed herein do not necessarily state or reflect those of the United States Government or the University of California, and shall not be used for advertising or product endorsement purposes.

Modeling Aerosol-Cloud Interactions with a Self-consistent Cloud Scheme in a General Circulation Model

Yi Ming[1], V. Ramaswamy[2], Leo J. Donner[2], Vaughan T.J. Phillips[2], Stephen A. Klein[3],

Paul A. Ginoux[2] and Larry H. Horowitz[2]

Abstract

This paper describes a self-consistent prognostic cloud scheme that is able to predict cloud liquid water, amount and droplet number (N_d) from the same updraft velocity field, and is suitable for modeling aerosol-cloud interactions in general circulation models (GCMs). In the scheme, the evolution of droplets fully interacts with the model meteorology. An explicit treatment of cloud condensation nuclei (CCN) activation allows the scheme to take into account the contributions to N_d of multiple types of aerosol (i.e., sulfate, organic and sea-salt aerosols) and kinetic limitations of the activation process. An implementation of the prognostic scheme in the Geophysical Fluid Dynamics Laboratory (GFDL) AM2 GCM yields a vertical distribution of N_d characteristic of maxima in the lower troposphere differing from that obtained through diagnosing N_d empirically from sulfate mass concentrations. As a result, the agreement of model-predicted present-day cloud parameters with satellite measurements is improved compared to using diagnosed N_d.

The simulations with pre-industrial and present-day aerosols show that the combined first and second indirect effects of anthropogenic sulfate and organic aerosols give rise to a global annual mean flux change of -1.8 W m^{-2} consisting of -2.0 W m^{-2} in shortwave and 0.2 W m^{-2} in longwave, as model response alters cloud field, and subsequently longwave radiation. Liquid water path (LWP) and total cloud amount increase by 19% and 0.6%, respectively. Largely owing to high sulfate concentrations from fossil fuel burning, the Northern Hemisphere mid-latitude land and oceans experience strong cooling. So does the tropical land which is dominated by biomass burning organic aerosol. The Northern/Southern Hemisphere and land/ocean ratios are 3.1 and 1.4, respectively. The calculated annual zonal mean flux changes are determined to be statistically significant, exceeding the model's natural variations in the NH low and mid-latitudes and in the SH low latitudes. Anthropogenic sulfate aerosol alone causes an annual mean flux change of -1.1 W m^{-2}.

1. Introduction

Clouds, which cover a significant fraction of the Earth's surface, play a critical role in affecting the radiation balance by partly reflecting the incoming shortwave sunlight back to space and by absorbing infrared radiation emitted by the surface. As highly dispersed systems made up of tiny droplets, water clouds can be characterized in terms of liquid water content (LWC) and droplet number concentrations (N_d). The corresponding cloud optical depth (τ) is approximately proportional to $LWC^{2/3}N_d^{1/3}$ [*Twomey*, 1977], indicating that the distribution of water mass among droplets has a direct bearing on the radiative properties of clouds. Such a mechanism is the origin of aerosol-cloud interactions and indirect effects of aerosols.

Soluble aerosol particles can be activated into droplets as cloud condensation nuclei (CCN) through dissolution – allowing water condensation to occur at a relatively low supersaturation. As a variety of natural and anthropogenic sources increase CCN concentrations, higher N_d not only make clouds more reflective by increasing cloud albedo (the first indirect effect), but also lengthen cloud lifetime by suppressing precipitation (the second indirect effect). Both effects may also lead to a weakening of the hydrological cycle [*Ramanathan et al.,* 2001]. The complexity and our relatively poor understanding of aerosol-cloud interactions contribute to the persisting uncertainties associated with the estimated radiative impacts of indirect effects [*Ramaswamy*, 2001]. For example, *Lohmann and Feichter* [1997] reported that the first and second indirect effects together can cause a global annual mean top-of-the-atmosphere (TOA) flux change ranging from -1.4 to -4.8 W m^{-2}, depending on the parameterizations of cloud cover and autoconversion.

Any effort to incorporate aerosol-cloud interactions into general circulation models (GCMs) naturally involves the task of relating N_d to aerosol properties (e.g., mass concentration, size distribution, chemical composition, solubility and surface activity) important for determining CCN efficiency. As one of the early attempts, *Boucher and Lohmann* [1995] (hereinafter referred to as BL95) proposed an empirical sulfate-N_d relationship by fitting measured/inferred N_d to sulfate mass concentrations. The relationship was adopted by a number of GCM studies of indirect effects (e.g., *Lohmann and Feichter*, 1997; *Rotstayn*, 1999; *Kiehl et al.*, 2000; *Ming et al.*, 2004a], and led to remarkably similar results. Nonetheless, the large scatter in the measured N_d used in BL95 is an indication of controlling factors other than the sulfate mass concentration, implying that BL95 may oversimplify the aerosol-N_d linkage.

The more recent and physically based approaches used in *Ghan et al.* [1997] and *Lohmann et al.* [1999] explicitly accounted for the meteorological and microphysical processes involved in droplet evolution as source and sink terms of prognostic schemes of N_d in GCMs. As the single most important source for N_d, the rates of CCN activation were calculated using the parameterizations of *Abdul-Razzak and Ghan* [2000] and *Chuang and Penner* [1995], respectively, which factored in the influence of aerosols and updraft velocity on the highly nonlinear process by fitting parcel model simulations. These studies assumed that most sink processes remove cloud liquid water and droplets proportionally. Hence the fractional removal rates for N_d were the same as those for liquid water, a common prognostic variable in GCMs.

In the atmosphere, cloud liquid water and droplets are produced and dissipated simultaneously, as they describe different aspects of the same process. No matter which meteorological process (e.g., large-scale ascent, radiative cooling, turbulent cooling and convection) causes cloud formation at a particular time and location, the same driving force must be responsible for the production of droplets as well as cloud liquid water. This seemingly plain real-world observation poses a fundamental constraint of self-consistency on any prognostic scheme used for simultaneously tracking cloud liquid water and droplets (in some cases, cloud amount as well). For example, all the prognostic variables should share the same source and sink terms. If cloud water detrained from convective updrafts contributes to stratiform clouds, the droplets contained in detrainment ought to be accounted for accordingly. Also, all the variables should be driven by exactly the same processes. It is not justifiable to use different updraft velocities for cloud liquid water and droplets.

This paper proposes a self-consistent prognostic scheme of cloud liquid water, amount and droplets. The predicted geographical and vertical distributions of prognosed N_d from an implementation of the scheme in the Geophysical Fluid Dynamics Laboratory (GFDL) AM2 GCM are compared with those diagnosed using BL95 [*Ming et al.*, 2004a]. The predicted cloud parameters are compared with satellite measurements. The combined first and second indirect effects are quantified using the difference in TOA radiation flux, whose statistical significance is assessed by comparing with the model's unforced variations.

2. Description of Scheme

2.1. Prognostic Equation for Cloud Droplet Number Concentration

An earlier version of the GFDL AM2 GCM [*Ming et al.*, 2004a] employed a variant of the cloud scheme of *Tiedtke* [1993] that was adapted for predicting cloud liquid water (l) and amount (a) in GCMs, while diagnosing N_d from the sulfate mass concentration. The new cloud scheme largely retains the treatment of l and a, and adds the air mass-based droplet number concentration (n) as a third prognostic variable (cloud ice is a separate prognostic tracer). Note that n is defined as the number of droplets per unit air mass (cloudy and clear together) as opposed to N_d that is defined on the basis of unit cloudy air volume (in-cloud), and is often used in reporting in-situ measurements. For a grid box, n can be converted to N_d following

$$N_d = \frac{n\rho_a}{a}, \tag{1}$$

where ρ_a is air density.

By explicitly accounting for the processes that contribute to droplet formation and dissipation, we arrive at the governing equation for n:

$$\frac{\partial n}{\partial t} = \left.\frac{\partial n}{\partial t}\right|_{ad} + \left.\frac{\partial n}{\partial t}\right|_{tu} + \left.\frac{\partial n}{\partial t}\right|_{cv} + \left.\frac{\partial n}{\partial t}\right|_{ls}. \tag{2}$$

$\left.\frac{\partial n}{\partial t}\right|_{ad}$ and $\left.\frac{\partial n}{\partial t}\right|_{tu}$ represent the advective and turbulent transport of droplets across the boundaries of model grid boxes. The convective and large-scale sources and sinks are denoted by $\left.\frac{\partial n}{\partial t}\right|_{cv}$ and $\left.\frac{\partial n}{\partial t}\right|_{ls}$, respectively.

2.2. Convective Source

The GFDL AM2 GCM uses the Relaxed Arakawa-Schubert (RAS) scheme [*Moorthi and Suarez*, 1992; *Anderson et al.*, 2003] to calculate the contribution of water detrainment from convective updrafts to cloud condensate. Detrainment from each updraft member j is assumed to occur only at cloud top. Consequently, one can write in analogy to the liquid source term:

$$\left.\frac{\partial n}{\partial t}\right|_{cv,i} = \sum_j \left(D^j (n_{tp}^{*j} - n_i) + gM_i^j \frac{\partial n_i}{\partial p} \right), \tag{3}$$

where n_{tp}^{*j} is the droplet number concentration in the convective updraft j at cloud top if it happens to detrain at layer i (i.e., cloud top is at layer i). n_i is the droplet number concentration in the environment at layer i. M_i^j is the corresponding convective mass flux. p and g are pressure and the gravitational constant, respectively. The mass detrainment rate, D^j, can be calculated as

$$D^j = \frac{gM_{tp}^j}{\Delta p_{tp}}, \tag{4}$$

The assumption of no detrainment at layers beneath cloud top and conservation of droplet number lead to:

$$M_{tp}^j n_{tp}^{*j} = (1 - r^j)(M_{ba}^j n_{cv-ac,ba}^j + \sum_{i=ba+1}^{tp-1} (M_i^j - M_{i-1}^j)((1-a)n_{cv-ac,i}^j + n_i)), \tag{5}$$

where $n_{cv-ac,ba}$ represents the number concentration of droplets activated at the base of a convective cloud, while $n_{cv-ac,i}$ is for those generated from activating CCN entrained at a particular layer i above cloud base. r^j represents the fraction of droplets that is removed through precipitation, and is assumed to be a function of detrainment pressure (see Appendix).

An assumption of Eq. 5 is that both clear and cloudy air can be entrained with probability of $1-a$ and a, respectively. Eq. 5 also implies that CCN that are not activated at the time of being entrained will remain unactivated all the way toward cloud top. This is a hypothesis that can be justified on the basis that experimental and modeling evidences suggest that typically the supersaturation within a cloud arrives at a maximum fairly close to the base, and then decreases monotonically with height (see Section 2.4) [*Pruppacher and Klett*, 1997]. So, immediately following the initial activation, the supersaturation decreases as an air parcel is transported vertically in a convective updraft, thus precluding further activation.

2.3. Stratiform Source/Sinks

Large-scale ascent, turbulent and radiative cooling may give rise to stratiform clouds by saturating air. Following the formulation of *Tiedtke* [1993], cloud droplet number shares the same large-scale sources and sinks as liquid water and amount. The term $\left.\frac{\partial n}{\partial t}\right|_{ls}$ in Eq. 2 is written as:

$$\left.\frac{\partial n}{\partial t}\right|_{ls} = \left.\frac{\partial n}{\partial t}\right|_{ls-ac} + \left.\frac{\partial n}{\partial t}\right|_{ev} + \left.\frac{\partial n}{\partial t}\right|_{er} + \left.\frac{\partial n}{\partial t}\right|_{au} + \left.\frac{\partial n}{\partial t}\right|_{ac} + \left.\frac{\partial n}{\partial t}\right|_{fr} + \left.\frac{\partial n}{\partial t}\right|_{ri} + \left.\frac{\partial n}{\partial t}\right|_{bf}, \quad (6)$$

where the $\frac{\partial n}{\partial t}$ terms with the subscripts $ls-ac$, ev, er, au, ac, fr, ri and bf refer to gain/loss in droplet number due to large-scale activation, evaporation, erosion, autoconversion, accretion, freezing, riming and the Bergeron–Findeisan process, respectively. Note that the term "evaporation" specifically refers to evaporation of droplets due to large-scale descent and warming, as opposed to "erosion" that describes evaporation caused by horizontal mixing of saturated and unsaturated air.

Since CCN activation occurs only in the newly formed cloudy fraction of a grid box, the contribution of large-scale activation can be expressed as:

$$\left.\frac{\partial n}{\partial t}\right|_{ls-ac} = n_{ls-ac} \left.\frac{\partial a}{\partial t}\right|_{ls-ac}, \tag{7}$$

where n_{ls-ac} is the droplet number concentration of new or incremental cloud amount. The time derivative of a ($\left.\frac{\partial a}{\partial t}\right|_{ls-ac}$) can be calculated following *Tiedtke* [1993].

This study treats the impact of large-scale descent and warming on droplets differently from that on cloud water. The resulting warming can partly evaporate cloud water, but cannot dissipate droplets unless a cloud is completely dissipated as a result. This is consistent with the treatment of cloud amount in *Tiedtke* [1993]. We assume that cloud erosion and all microphysical processes, namely autoconversion, accretion, freezing, riming and the Bergeron–Findeisan process, remove cloud droplets and liquid water proportionally. Hence an existing parameterization that is formulated for cloud water in terms of fractional removal can be applied to droplets without modification.

2.4. Parameterization of Activation and Other Microphysical Processes

It is important to distinguish CCN activation in the absence of pre-existing droplets from that in their presence for convective clouds. Initial activation at cloud base belongs to the former case. Then, when the droplets produced at cloud base are carried upwards in a convective system, they compete for water with entrained CCN in a way that suppresses supersaturation, and subsequently affects the concentration of newly formed droplets (the latter case).

Without pre-existing droplets, the concentration of activated droplets is a function not only of aerosol size distribution and chemical composition, but also of updraft velocity, which varies from a few meters per second for convective clouds to as low as a fraction of a centimeter per second for stratiform clouds. The tremendous range of updraft velocity poses a serious challenge for any effort to parameterize the highly nonlinear activation process, especially at low updraft and/or high aerosol concentrations (i.e., conditions favorable for kinetic limitations). Given that, this study utilizes the parameterization proposed by *Ming et al.* [2004b] because of its satisfactory performance over a wide range of updraft velocity to calculate $n_{cv-ac,ba}$ in Eq. 5 and n_{ls-ac} in Eq. 7. Because the RAS scheme does not resolve the vertical profile of updraft velocity, the average updraft velocity in an ensemble of convective clouds is approximated at $0.5\sqrt{CWF}$, where cloud work function (CWF) is the integral of buoyancy along the path of convection. By doing so, convective updraft velocity is linked to cloud type. The scaling factor of 0.5 is used to approximately account for the fact that a convective updraft may accelerate along the path. The turbulent and radiative cooling rates calculated from the GCM are converted to equivalent updraft velocities, which are added to the actual model-resolved grid-mean velocity of large-scale ascent outside of convective updrafts and downdrafts to form a composite updraft velocity used for activation.

Here, we propose an approach to quantifying the contribution to droplets of continual activation above convective cloud base. For an entraining air parcel rising at a velocity of V, the time derivative of the supersaturation s obeys:

$$\frac{ds}{dt} = \alpha' V - \gamma \frac{dW_L}{dt}, \tag{8}$$

where W_L is the concentration of cloud liquid water (unit: kg(water) m^{-3}(air)). The coefficients α' and γ depend on the concentration of water vapor and temperature of the cloud (W_V and T, respectively) and of the environment (W_V' and T', respectively) as well as the entrainment rate (μ):

$$\begin{aligned} \alpha' &= \frac{gM_w\Delta H_v}{C_{pa}RT^2} - \frac{gM_a}{RT} \\ &+ \frac{M_w \Delta H_v \mu}{RT^2}\left[\frac{\Delta H_v}{C_{pa}\rho_a}(W_V - W_V') + (T - T')\right] \\ &- \left[\frac{RT}{p_s M_w} + \frac{M_w \Delta H_v^2}{C_{pa} p M_a T}\right]\mu(W_V - W_V' + W_L), \end{aligned} \tag{9}$$

and

$$\gamma = \frac{RT}{p_s M_w} + \frac{M_w \Delta H_v^2}{C_{pa} p M_a T}, \tag{10}$$

The physical parameters involved in Eqs. 9 and 10 are the universal gas constant, R, the molecular weight of water, M_w, the latent heat of water, ΔH_v, the heat capacity of air, C_{pa}, the molecular weight of air, M_a, and the saturated vapor pressure of water, p_s.

It is a good assumption that the amount of water condensing onto droplets is significantly larger than that onto interstitial particles after the initial activation at cloud base finishes. Thus the condensation rate can be expressed as:

$$\frac{dW_L}{dt} = \frac{\pi}{2}\rho_w G(D_d)(s - s_{eq})D_d n, \tag{11}$$

where D_d and n are the average diameter and number concentration of droplets, respectively. s_{eq} is the equilibrium supersaturation of droplets. The growth coefficient G depends on droplet size. ρ_w is water density.

A common characteristic of the profiles of supersaturation simulated with a parcel model [*Ming and Russell*, 2004] and plotted in Fig. 1 is that after reaching a maximum at cloud base (the bottom 10 m or so), it levels off rapidly, and keeps on decreasing at a pace as slow as 10^{-5} s^{-1}, thus entering a pseudo-equilibrium state and making it plausible to assume $\frac{ds}{dt} = 0$ numerically. By bringing Eq. 11 into Eq. 8 and setting its left-hand side to zero, we can solve for the pseudo-equilibrium s. We further assume that among the newly entrained CCN, only those whose critical supersaturation is lower than the calculated s will be activated. This approach is used to calculate $n_{cv-ac,i}$ in Eq. 5.

Cloud erosion follows the same expression as in *Tiedtke* [1993], and the rate constant is higher in convective and turbulent conditions (see Appendix). The parameterization of the microphysical processes largely follows *Rotstayn* [1997] and *Rotstayn et al.* [2000]. As the only exception, autoconversion is calculated according to the work of *Khairoutdinov and Kogan* [2000], which considers the continuous effect of N_d.

2.5. Implementation of Scheme in GCM

The new cloud scheme is implemented in the GFDL AM2 GCM. A detailed overview of model structure and validation is provided by *Anderson et al.* [2003]. The prescribed sea surface temperature (SST) simulations described in this paper are run at a horizontal resolution of N45 (2.5° in longitude × 2° in latitude) and with 24 vertical layers which lie mostly in the troposphere. All the runs discussed in this study cover a duration of 6 years with the first year as spin-up. The aerosol climatology used in the GCM is prescribed by interpolating monthly mean 3-dimensional distributions of mass concentrations calculated off-line with a chemistry transport model, and thus does not interact with the model meteorology. The aerosol species are assumed to be externally mixed, and share the same size distribution consisting of two log-normal modes (N_1:N_2=17:3 $D_{g,1}$=0.01 μm σ_1=1.6 $D_{g,2}$=0.07 μm σ_2=2.0) [*Whitby et al.,* 1978], which is represented with 40 logarithmically-spaced equal size bins in the GCM. Sulfate and sea-salt aerosols are treated as $(NH_4)_2SO_4$ and NaCl, respectively, while organic aerosol is modeled as a mixture of four soluble compounds including malic acid (48% by mass), citric acid (22%), glucose (4.8%) and fructose (4.7%), and a generic insoluble species (20.5%). This composition was used to study hygroscopic growth and CCN efficiency of organic aerosol [*Ming and Russell,* 2001; 2004]. Surface-active organic aerosol can lower droplet surface tension below that of pure water, and the relationship between surface tension and total concentration of organic species in droplets used in the parameterization of CCN activation is derived from the measurements of *Facchini et al.*

[2000]. The Appendix lists the values of model parameters and describes the numerical method used in integrating the governing equation for the stratifrom source/sinks (Eq. 6).

3. Results

3.1. Column Burdens

The monthly mean aerosol climatology of sulfate and organic carbon (OC) is generated using the Model for OZone AND Related chemical Tracers (MOZART) [*Tie et al.,* 2001; *Horowitz et al.,* 2003; *Tie et al.,* 2005]. The total mass concentration of coarse and fine sea-salt is related to Special Sensor Microwave Imager (SSMI)-observed monthly mean surface wind speed [*Haywood et al.,* 1999]. Since fine particles account for most CCN in terms of number, this study uses a fraction of 10% to derive concentration of fine sea-salt from total concentration [*O'Dowd et al.,* 1997]. The pre-industrial (PI) and present-day (PD) geographical distributions of column burdens in January and July are plotted in Fig. 2.

Largely resulting from burning sulfur-containing fossil fuels, the highest PD burdens of sulfate aerosol center over the Northern Hemisphere (NH) mid-latitude industrial regions, namely East Asia, Europe and United States. Long-range transport of continental emissions considerably elevates the concentrations over the NH oceans, namely North Pacific and North Atlantic. The seasonal variations are strong with the burden in July significantly higher than in January. The biogenic nature of PI sulfate causes higher burdens in lower latitudes and during summertime. The PI and PD global annual mean sulfate burdens are 0.22 and 0.81 Tg S, respectively. Both fossil fuel and biomass burning gives rise to PD OC. The three industrial source regions of sulfate have some of the highest OC burdens, the rest of which occur over the regions characteristic of heavy biomass burning, namely India, Central Africa and South America. The global annual mean OC burden is 0.17 Tg for PI and 1.36 Tg for PD. An Organic Matter (OM)/OC ratio of 1.4 is used to convert the burden of OC to that of OM. The PI and PD burdens of naturally-occurring sea-salt are assumed to be the same, and are highest over the oceanic regions with high wind speed. The global annual mean burden of fine sea-salt is 0.02 Tg.

3.2. Distributions of N_d

Fig. 3 depicts the geographical distribution of in-cloud N_d at 904 mb from a simulation with the prognostic cloud scheme driven by the PD aerosol climatology. The corresponding tendencies of convective and large-scale sources and sinks are plotted in Fig. 4. In January, relatively high N_d (over 100 cm^{-3}) are seen over the tropical and subtropical oceans and land, especially the regions off the coast of East and South Asia, Africa, and South America, where droplets form mainly from convection (Fig. 4). In contrast, the large-scale processes over the NH mid-latitude land are generally weaker, producing N_d less than 50 cm^{-3}. These are smaller than 100 - 150 cm^{-3} diagnosed from sulfate mass concentrations using BL95. Because the measurements presented in *Leaitch* [1992] showed strong seasonal variations and were used as the only dataset in fitting the sulfate-N_d relationship over land of BL95, N_d in January diagnosed using BL95 may have positive biases. The discrepancy may also be partly due to underestimation of sulfate burdens in January by MOZART. In July, not only the convectively active regions in tropics and subtropics, but also the mid-latitude NH land and oceans have N_d frequently over 100 cm^{-3} as a result of increased aerosol concentrations. While sharing a similar range, diagnosed N_d are generally higher than prognosed N_d.

A closer look at Figs. 3 and 4 reveals an interesting yet seemingly counterintuitive feature that strong tendency of sources does not necessarily lead to higher N_d. For example, despite the strong convection over the SH subtropical oceanic region off the west coast of Africa in July, the equilibrium N_d are less than 10 cm^{-3}. The explanation lies in the second indirect effect. Because lower N_d have a tendency to accelerate cloud dissipation and shorten lifetime, droplets form more frequently than at higher N_d. So, even though N_d are low due to the lack of CCN, the enhanced frequency of cloud formation/dissipation gives rise to strengthening of source tendency.

The vertical distribution of zonal mean N_d is shown in Fig. 5. As droplet evolution interacts with the model meteorology, N_d simulated with the prognostic scheme exhibit a vertical structure distinct from diagnosed N_d, for which the signature of vertical transport of ground-based emissions with maxima adjacent to the surface is clearly borne out. As an overall trend, prognosed N_d increase with altitude starting from the surface, and then decrease after reaching maxima approximately at 800 mb. This is mainly because convective detrainment of cloud water and associated droplets occurs at these pressure levels, as opposed to at the surface. N_d gradually decrease to less than 10 cm^{-3} for the water fraction of mixed-phase clouds above the boundary layer. In contrast, diagnosed N_d are not constrained by the boundary layer, and could be as high as 100 cm^{-3} for mixed-phase clouds. Since the field measurements on which the empirical relationship of BL95 is based were taken for low-altitude warm clouds, its applicability to mixed-phases clouds is uncertain, especially given the differing meteorological conditions of the two cloud types.

3.3. Comparison with Satellite Measurements

We use the GCM with prognostic treatment of N_d to simulate the PD liquid water path (LWP) over ocean. The results in January are characteristic of two major peaks at 30°N and 45°S and two others close to the equator, a pattern similar to that in the SSMI measurements [*Greenwald et al.*, 1995; *Weng and Grody*,1994] (Fig. 6). The simulated LWP is generally in good agreement with the observations in both hemispheres, but underestimates in the high latitudes. The model accurately catches the increase in LWP in the NH mid-latitudes in July, while underestimating LWP in the tropics and in the SH mid-latitudes. In contrast, the use of diagnosed N_d yields much higher LWP compared to prognosed N_d, and worsens the agreement with measurements. Most notably, the model with diagnosed N_d overestimates LWP almost by a factor of 3 in the NH mid-latitude in July. This is because diagnosed N_d are much higher than prognosed N_d, and tend to prolong cloud lifetime and elevate LWP by suppressing precipitation.

The GCM-simulated PD cloud optical depth is compared with the International Satellite Cloud Climatology Project (ISCCP) measurements in Fig. 7. Note that logarithmic (as opposed to linear) averaging is applied to computing the monthly mean cloud optical depth since the change in irradiance measured by satellites and used in deriving cloud optical depth is less sensitive to optically thick clouds than thin clouds as a result of saturation. The measured cloud optical depth is relatively uniform in the low latitudes both in January and in July. The model predictions are typically twice as high as the measurements. The general trend of the ISCCP data in the mid-latitudes is that cloud optical depth increases with latitude, opposite to what the model suggests except in the NH summertime. Overall the agreement is within a factor of 2. The overestimation caused by using diagnosed N_d in the NH mid-latitude in July is almost a factor of 4.

Except in the high latitudes, the GCM-predicted total cloud amount largely repeats the latitudinal pattern of the ISCCP measurements (Fig. 8). The model underestimates total cloud amount by less than 10% in the Southern Hemisphere (SH) mid-latitudes in January, and in the NH mid-latitudes and in the SH low latitudes in July. The different schemes of N_d cause little change in total cloud amount.

The PD shortwave (SW) and longwave (LW) cloud forcings diagnosed from the GCM are shown in Figs. 9 and 10, respectively. The prognostic cloud scheme achieves a satisfactory agreement between the model predictions and Earth Radiation Budget Experiment (ERBE) measurements in terms of shortwave cloud forcing, thus enhancing our confidence in the scheme's ability in representing PD radiative effects of clouds with aerosol impact explicitly accounted for, and, furthermore, in establishing a baseline simulation that can be readily perturbed to study indirect effects. In contrast, an overestimation of 38 W m^{-2} in shortwave cloud forcing occurs at 55°N in July when diagnosed N_d are used. This is not nearly as significant as in the case of LWP in terms of percentage increase largely due to the nonlinearity of the relationship between radiation and LWP. The model's underestimation of total cloud fraction also partly compensates for the overestimated LWP.

3.4. Flux Changes

The difference in TOA radiation flux between two simulations with the prognostic cloud scheme driven separately by PI and PD aerosol climatology is employed to assess the sign and scale of indirect effects (designated as the BASE case). The aerosol climatology used for clear-sky calculation remains the same at the PD level in both runs, and thus neither direct nor semi-direct effect is included. Note that both runs allow the model meteorology to evolve, so the calculated flux change is the measure of combined first and second effects, and includes the impact of model feedback mechanisms [*Ming et al.*, 2004a]. As seen in Fig. 11, owing to the response of the model to the change in N_d, regional warming scatters across the globe, especially over the SH oceans and Australia as a result of altered local circulation. Nonetheless, cooling typically ranging from -3 to -10 W m^{-2} is found over the NH mid-latitude industrial regions because of high burdens of sulfate and organic aerosols. Strong cooling is also wide-spread over the NH oceans as a result of long-range transport of continental aerosols. Mainly due to high burdens of biomass burning OC, the tropical parts of South America and Africa undergo cooling, which largely ranges from -5 to -20 W m^{-2}, even stronger than that over the sulfate-dominant industrial regions. The global annual mean flux change amounts to -1.8 W m^{-2} including a SW component of -2.0 W m^{-2} and a LW component of 0.2 W m^{-2} (Table 1). The NH/SH and land/ocean ratios are 3.1 and 1.4, respectively.

The geographical distributions of the flux changes in SW and LW are plotted in Fig. 12. The SW cooling is stronger and more wide-spread than when SW and LW are combined. In particular, parts of Russia and Canada at around 60°N, where concentrations of anthropogenic aerosols are relatively low, have cooling approximately as strong as the source regions, but the LW warming largely cancels out the SW cooling, different from the source regions. In contrast, the LW components of flux changes are relatively small over ocean, and the total flux changes are largely in SW.

Higher prognosed N_d incur a percentage increase in annual mean LWP of 19% (from 47 g m^{-2} for PI to 56 g m^{-2} for PD), while the increase in total cloud amount is 0.6% (from 64.6% for PI to 65.0% for PD). As shown in Fig. 13, the largest increases in LWP occur over the NH mid-latitude industrial regions and oceans as well as over the tropical biomass burning regions. When diagnosed N_d are used, the global annual mean LWP changes from 70 g m^{-2} for PI to 78 g m^{-2} for PD, representing an increase of 11%. The increased LWP centers predominantly in the sulfate-dominant NH mid-latitudes since BL95 only considers the impact of sulfate aerosol.

3.5. Role of OC in Aerosol-Cloud Interactions

Numerous experimental and modeling studies [e.g., *Cruz and Pandis,* 1997; *Corrigan and Novakov,* 1999; *Russell et al.,* 2000] have indicated that soluble and/or surface-active OC can be efficient CCN. The prognostic cloud scheme employs a parameterization of CCN activation that has been shown to be able to satisfactorily represent OC [*Ming et al.*, 2004b]. In a sensitivity case designed to evaluate the role of OC in aerosol-cloud interactions on the global scale (the NOOC case), the PI and PD prescribed SST simulations are re-run with only sulfate and sea-salt aerosols, and the calculated flux changes are plotted in Fig. 14. The omission of OC considerably weakens the cooling over the tropical parts of Central Africa and South America, where high burdens of biomass burning OC are located (Fig. 2). In the NH mid-latitudes, the cooling is also reduced but to a lesser extent because indirect effects are largely due to sulfate aerosol. The resulting global annual mean flux change is -1.1 W m^{-2} as compared to -1.7 W m^{-2} in BASE and -2.3 W m^{-2} calculated from N_d diagnosed with BL95 [*Ming et al.,* 2004a] (Table 1). As shown in Fig. 14, the geographical pattern of the flux change calculated using diagnosed N_d differs from the NOOC case to a large extent. While both cases yield comparable cooling over the NH mid-latitude land, the cooling over the oceans in NOOC is not nearly as strong as suggested by using diagnosed N_d. The underlying reasons for the differences are discussed in Section 4.3.

3.6. Confidence Levels

The model's natural variability is responsible for inherent fluctuation of radiation flux, which may reduce the confidence levels in the flux change resulting from perturbation in aerosol climatology. In Fig. 15, the model's zonal mean natural variations are represented by the standard deviations estimated from a total of 20-year simulation with aerosol climatology unchanged at PI or at PD level. For this particular version of the GFDL GCM, relatively large variations can be found near to the equator and in the high latitudes, while the variations are generally less than 1 W m^{-2} in the low and mid-latitudes. The calculated zonal mean flux changes in BASE exceed the standard deviations to various extents in the NH low and mid-latitudes and in the SH low latitudes, implying that the probability of these flux changes being forced perturbations as opposed to natural variations is at least greater than 68%. In the NH mid-latitudes, where the strongest cooling is located, the flux changes are approximately two times greater than the corresponding standard deviations, effectively ruling out the possibility that they are caused by the model's natural variability. Similar to BASE, the NOOC case yields unambiguous flux changes in the NH mid-latitudes, but considerably weakens flux changes in the SH low latitudes to levels comparable to or less than standard deviations. This confirms the significant role played by OC in aerosol-cloud interactions over the biomass burning regions.

4. Discussion

4.1. Breakdown of First Indirect Forcing Concept

It is a common view that the first indirect effect is suitable for being quantified using the well-defined "forcing" concept. In the studies that diagnose N_d directly from aerosol concentrations [e.g., *Ming et al.,* 2004a], the first indirect forcing is calculated as the difference in radiation flux or cloud radiative forcing caused by perturbation in aerosol, which instantaneously translates into change in N_d. In contrast, in a prognostic cloud scheme like the one presented in this paper, which represents a more realistic linkage between aerosols and N_d, the characteristic timescale for N_d to reach equilibrium after perturbing aerosol climatology (hours) is longer than the model time step (30 minutes). In other words, meteorological fields evolve before new aerosols fully affect N_d, thus violating the rigorous definition of "forcing". Therefore, it is not possible to calculate first indirect forcing if N_d are being determined prognostically.

4.2. Subgrid Variability of Updraft Velocity

Owing to convection and large-scale processes, the upward motion of moist air is the fundamental driving force behind cloud formation. Critical for prognostic determination of cloud water as well as droplet number in GCMs, updraft velocity (w) can be thought of as the summation of grid-mean ($\bar{w}$) and subgrid variation (w'). In reality, it is w that drives cloud formation, but only grid-mean $\bar{w}$ can be resolved from GCMs. In the earliest study of prognostic scheme of N_d, *Ghan et al.* [1997] argued that since w' is necessary for accounting for the impact of subgrid variability of w on CCN activation, its probability distribution can be diagnosed either from the turbulent kinetic energy (TKE) or from the vertical eddy diffusivity (K) and relating the standard deviation of w (σ_w) to TKE. A simpler method used in *Lohmann et al.* [1999] assumed $w = \bar{w} + c\sqrt{TKE}$ with c empirically set at 0.7. Also, *Ghan et al.* [1997] did not distinguish convective and large-scale sources of cloud droplets, and *Lohmann et* *al.* [1999] effectively omitted possible aerosol impact on convective source by assuming a constant radius of 10 μm for these droplets.

If approaches similar to those of *Ghan et al.* [1997] and *Lohmann et al.* [1999] are applied to the GFDL GCM, which uses grid-mean $\bar{w}$ to drive cloud formation, the inconsistency in updraft velocity poses a fundamental problem in that the same updraft field should drive both cloud droplet growth and liquid water increase simultaneously, whether subgrid variability is explicitly considered or not in a GCM. In other words, if subgrid components of w are taken into account in determining N_d, the impact on l ought to be fully accounted for. This insight can be further illustrated with a thought experiment. If the requirement of consistency is not met, the combination of a zero $\bar{w}$ and a non-zero w' would allow droplets to be formed in the absence of cloud liquid water, projecting an unphysical picture.

This study approaches the issue of subgrid variability by first drawing upon observations of the real atmosphere and recognizing that two major types of updraft (i.e., convective and large-scale) operate. Rather rapid ascents take place in convective systems, and w can reach a few meters per second, while relatively slow large-scale updrafts are on the order of centimeter per second. Approaches developed for modeling convection (e.g., the RAS convection scheme used here) treat ensembles of convective clouds, and enable subgrid variability of w resulting from convection to be fully accounted for. In the case of large-scale stratiform clouds, the choice of grid-mean $\bar{w}$ for calculating CCN activation allows us to apply the same w to forming cloud water and droplets. This method is further supported by the argument that the impact of subgrid variability of w on CCN activation may be negligible in some situations. Two conditions must be met for the argument to be valid. First, the activation process is linear with respect to w. Second, w does not affect the probability of cloud formation (i.e., the subgrid distribution of clouds is independent of w). As plotted in Fig. 16, a test case reveals that activated droplet numbers increase approximately linearly with updraft velocity from 0.1 to 6 cm s^{-1} (typical for large-scale ascent), satisfying the first condition. The independence between w and clouds can be tentatively justified from the consideration that whether a cloud will form or not at a particular time and location probably depends more on relative humidity than on weak cooling resulting from large-scale processes. So, it is reasonable to use grid-mean $\bar{w}$ to drive CCN activation when w is relatively low. Of course, not in all situations are both conditions met. For example, relatively high updraft velocity may lead to cloud formation by saturating an air parcel whose relative humidity is initially well below 100%, thus violating the second condition. Nonetheless, this analysis helps explain why our prognostic scheme can produce enough droplets to sustain LWP at levels comparable to measurements. Our approach can account for the impact on N_d of subgrid variability of w to some extent without having to diagnosing subgrid variability empirically, and represents a reasonable alternative to the previous ones of *Ghan et al.* [1997] and *Lohmann et al.* [1999].

Though this study has to estimate updraft velocity in an ensemble of convective clouds from CWF as the RAS scheme is unable to resolve its vertical structure, such a method differs fundamentally from deriving subgrid variations from grid-mean TKE and applying them to driving large-scale stratifrom clouds. The limitation posed by diagnosing convective updraft from CWF can be readily overcome since an explicit vertical distribution of updraft is well within the reach of an improved convection scheme.

4.3. Comparison with Other Studies

Numerous studies, including the most recent one by *Ming et al.* [2004a], used the empirical relationship of BL95 relating N_d to mass concentrations of sulfate (a surrogate for all aerosols) to simulate indirect effects. *Ming et al.* [2004a] reported a global annual mean flux change of -2.3 W m^{-2}, stronger than -1.1 W m^{-2} in the NOOC case of this study (we believe that NOOC is more appropriate for comparison than BASE since the BL95 relationship does not account for OC explicitly). In light of the sharp contrast between the simplistic nature of BL95 and layers of complexity surrounding the prognostic scheme, the difference of 1.2 W m^{-2} and distinct geographical patterns (Fig. 14) are not unexpected, but still prompt a further investigation of the practicality of BL95, with the assistance of the prognostic cloud scheme used here.

Scatter plots of predicted N_d and corresponding sulfate concentrations at the grid points located from 20°N to 60°N in BASE are given in Fig. 17. These latitudes cover all the major industrial regions (i.e., East Asia, Europe and the United States), and are characteristic of relatively high sulfate burdens (Fig. 2). Because BL95 was fitted from field data gathered in North America and North Atlantic, it presumably reflects sulfate-N_d correlation in these sulfate-dominant regions, if there is such a correlation. It can be seen from Fig. 17 that a large scatter is associated with prognosed N_d for sulfate concentrations from 0.1 to 10 μg m^{-3}, spanning almost two orders of magnitude from 10 to 1000 cm^{-3}. This suggests that sulfate is not the sole determinant of N_d in the prognostic scheme. Nonetheless, the general trend appears to be that N_d increase with the sulfate mass concentration both over ocean and over land, reaffirming the major role of sulfate in providing CCN for cloud formation. Despite the overestimation of BL95 compared to the model predictions over land, the slope of mean N_d, which dictate the relative increases in N_d due to anthropogenic sulfate aerosol, and subsequently the flux changes, are rather similar to BL95. This is the characteristic mainly responsible for the similar indirect effects over the NH mid-latitude land calculated with prognosed N_d as well as with diagnosed N_d. In contrast, mean N_d over ocean do not show strong dependence on the sulfate mass concentration except when it is lower than 0.3 μg m^{-3}, implying that marine clouds may not be as susceptible to aerosols as suggested by BL95. This explains why the cooling over the NH mid-latitude oceans in NOOC is much weaker than when diagnosed N_d are used. Fig. 18 is for OC-abundant 20°S to 20°N regions. Here, mean N_d even decrease with respect to the sulfate mass concentration when it is above 1 μg m^{-3}, as the presence of large amount of OC, which provides a significant fraction of CCN over this region, renders the dependence of N_d on sulfate less significant. So, BL95 may not be as applicable to the tropical and subtropical regions as to the mid-latitudes.

The prognostic schemes of N_d developed by *Ghan et al.* [1997] and *Lohmann et al.* [1999] have been utilized to estimate indirect effects of sulfate aerosol [*Ghan et al.,* 2001; *Lohmann et al.,* 2000]. The differences in the treatment of subgrid variability, parameterizations of activation and autoconversion, and other aspects of the schemes make it impossible to make a clean comparison of this study with the two previous ones. Instead, we reiterate some findings of *Ghan et al.* [2001] useful for putting this study into perspective. First, the large difference in the calculated indirect effects due to externally mixed anthropogenic sulfate aerosol between *Lohmann et al.,* [2000] (-0.1 W m^{-2}) and *Ghan et al.,* [2001] (-2.4 W m^{-2}) is attributable to the arbitrary lower limits on aerosol and droplet numbers. Note that this study avoids using such limits and differs from *Ghan et al.* [1997] (a lower limit on σ_w of 0.1 m s^{-1}) and *Lohmann et al.* [1999] (a background N_d value of 40 cm^{-3}) in this regard. This adds to the soundness of the prognostic scheme of this study as it completely eliminates the need for such artifacts. Second, *Ghan et al.* [2001] examined the sensitivity of indirect effects to aerosol numbers diagnosed with a fixed normalized distribution, as is the case for this study, and found that the flux change increases from -2.4 W m^{-2} with predicted aerosol numbers to -3.1 W m^{-2} with diagnosed aerosol numbers. The NOOC case of this study obtains a global annual mean shortwave flux change of -1.5 W m^{-2}, much weaker than what *Ghan et al.* [2001] found. The underlying reasons for the differences can be fully explained only by a carefully designed model intercomparison.

5. Conclusions

This paper describes a self-consistent prognostic cloud scheme that is capable of predicting cloud liquid water, amount and droplet number from the same model-resolved field of updraft velocity. The evolution of droplets fully interacts with the model meteorology. Explicitly treated as a major source of droplets, CCN activation is parameterized using the microphysically based approach proposed by *Ming et al* [2004b], which allows the scheme to take into account the impacts on N_d of multiple types of aerosol (i.e., sulfate, OC and sea-salt), decreased droplet surface tension due to OC, and kinetic limitations. An implementation of the scheme in the GFDL GCM yields a vertical structure of N_d characteristic of maxima at around 800 mb, as opposed to being adjacent to the surface for N_d diagnosed from sulfate mass concentrations using BL95. This can be attributed to detrainment of convection at higher altitudes. The agreement between model diagnostics and satellite-measured LWP, cloud amount and forcing is improved compared to using diagnosed N_d.

The simulations with PI and PD aerosols show that the combined first and second indirect effects of anthropogenic sulfate and organic aerosols give rise to a global annual mean flux change of -1.8 W m^{-2} consisting of -2.0 W m^{-2} in shortwave and 0.2 W m^{-2} in longwave, as model response alters cloud field, and subsequently longwave radiation. Specifically, LWP and total cloud amount increase by 19% and 0.6%, respectively. The cooling is centered over the NH mid-latitude industrial regions (i.e., East Asia, Europe, and United States) and oceans (i.e., North Pacific and North Atlantic) mainly due to sulfate aerosol, and over the tropical parts of South America and Central Africa mainly due to organic aerosol. The NH/SH and land/ocean ratios are 3.1 and 1.4, respectively. Exceeding the model's natural variations in the NH low and mid-latitudes and in the SH low latitudes, the calculated annual zonal mean flux changes are determined to be statistically significant. Sensitivity analyses show that anthropogenic sulfate alone gives rise to an annual mean flux change of -1.1 W m^{-2}, and the absence of organic aerosol significantly weakens the cooling over the tropical land.

Acknowledgements

Through the contributions of S. Klein, this work was performed under the auspices of the U.S. Department of Energy at the University of California Lawrence Livermore National Laboratory under contract #W-7405-Eng-48.

Appendix: Model Parameters and Numerical Integration

The threshold value of grid-mean relative humidity above which stratiform clouds start to form is set at 80%. This study assumes that convective precipitation removes water condensate and droplets proportionally. As a function of detrainment pressure, the removal fraction r^j in Eq. 5 is 0.5 below 800 m, 0.975 above 500 mb, and linearly interpolated at intermediate pressure levels. The cloud erosion rate constant is set at 4.7×10^{-6} s^{-1} in convective conditions, 5.0×10^{-5} s^{-1} in turbulent conditions, and 1.0×10^{-6} s^{-1} otherwise. The mass and heat accommodation coefficients used in the parameterization of CCN activation are both 1 [*Laaksonen et al.,* 2005].

Because the time step of the GCM cloud scheme (30 minutes) is much longer than the characteristic timescale of Eq. 6, analytical integration is necessary for its use in tracking droplet number. As large-scale activation is treated as constant and the other microphysical processes as linear to n, Eq. 6 turns into:

$$\left.\frac{\partial n}{\partial t}\right|_{ls} = E - Fn. \tag{12}$$

An analytical integration of Eq. 12 (analogous to that for l in *Tiedtke* [1993]) suggests that n at the time step $t + \Delta t$ can be related to n at the previous step t following:

$$n(t + \Delta t) = n(t)e^{-F\Delta t} + \frac{E}{F}(1 - e^{-F\Delta t}) \tag{13}$$

References

Abdul-Razzak, H., and S.J. Ghan, A parameterization of aerosol activation 2. Multiple aerosol types, *J. Geophys. Res., 105,* 6837-6844, 2000.

Anderson, J.L., V. Balaji, A.J. Broccoli, W.F. Cooke, T.L. Delworth, K.W. Dixon, L.J. Donner, K.A. Dunne, S.M. Freidenreich, S.T. Garner, R.G. Gudgel, C.T. Gordon, I.M. Held, R.S. Hemler, L.W. Horowitz, S.A. Klein, T.R. Knutson, P.J. Kushner, A.R. Langenhorst, N.C. Lau, Z. Liang, S.L. Malyshev, P.C.D. Milly, M.J. Nath, J.J. Ploshay, V. Ramaswamy, M.D. Schwarzkopf, E. Shevliakova, J.J. Sirutis, B.J. Soden, W.F. Stern, L.A. Thompson, R. John Wilson, A.T. Wittenberg, and B.L. Wyman, The new GFDL global atmosphere and land model AM2/LM2: Evaluation with prescribed SST simulations, *J. Clim.,* accepted, 2003.

Boucher, O., and U. Lohmann, The sulphate-CCN-cloud albedo effect - A sensitivity study with two general circulation models, *Tellus, 47B,* 281-300, 1995.

Cess, R.D., and G.L. Potter, A methodology for understanding and intercomparing atmospheric climate feedback processes in GCMs, *J. Geophys. Res., 93,* 8305-8314, 1988.

Chuang, C.C., J.E. Penner, K.E. Taylor, A.S. Grossman, and J.J. Walton, An assessment of the radiative effects of anthropogenic sulfate, *J. Geophys. Res., 102,* 3761-3778, 1997.

Chuang, C.C., J.E. Penner, J.M. Prospero, K.E. Grant, G.H. Rau, and K. Kawamoto, Cloud susceptibility and the first aerosol indirect forcing:

Sensitivity to black carbon and aerosol concentrations, *J. Geophys. Res., 107,* doi10.1029/2000JD000215, 2002.

Corrigan, C.E., and T. Novakov, Cloud condensation nucleus activity of organic compounds: a laboratory study, *Atmos. Environ., 33A,* 2661-2668, 1999.

Cruz, C.N., and S.N. Pandis, A study of the ability of pure secondary organic aerosol to act as cloud condensation nuclei, *Atmos. Environ., 31A,* 2205-2214, 1997.

Facchini, M.C., S. Decesari, M. Mircea, S. Fuzzi, and G. Loglio, Surface tension of atmospheric wet aerosol and cloud/fog droplets in relation to their organic carbon content and chemical composition, *Atmos. Environ., 34,* 4853-4857, 2000.

Leaitch, W.R., G.A. Isaac, J.W. Strapp, C.M. Banic, and H.A. Wiebe, The relationship between cloud droplet number concentrations and anthropogenic pollution: observations and climatic implications, *J. Geophys. Res., 97,* 2463-2474, 1992.

Ghan, S.J., L.R. Leung, R.C. Easter, and H. Abdul-Razzak, Prediction of cloud droplet number in a general circulation model, *J. Geophys. Res., 102,* 21777-21794, 1997.

Ghan, S.J., R.C. Easter, E.G. Chapman, H. Abdul-Razzak, Y. Zhang, L.R. Leung, N.S. Laulainen, R.D. Saylor, and R.A. Zaveri, A physically based estimate of radiative forcing by anthropogenic sulfate aerosol, *J. Geophys. Res., 106,* 5279-5293, 2001.

Han, Q., W.B. Rossow, and A.A. Lacis, Near-global survey of effective droplet radii in liquid water clouds using ISCCP data, J. Clim., 7, 465-497, 1994.

Haywood, J.M., V. Ramaswamy, and B.J. Soden, Tropospheric aerosol climate forcing in clear-sky satellite observations over the oceans, *Science, 283,* 1299-1303, 1999.

Horowitz, L.W., S. Walters, D.L. Mauzerall, L.K. Emmons, P.J. Rasch, C. Granier, X.X. Tie, J.-F. Lamarque, M.G. Schultz, G.S. Tyndall, J.J. Orlando, and G.P. Brasseur, A global simulation of tropospheric ozone and related tracers: Description and evaluation of MOZART, version 2, *J. Geophys. Res., 108,* doi:10.1029/2002JD002853, 2003.

Khairoutdinov, M., and Y. Kogan, A new cloud physics parameterization in a large-eddy simulation model of marine stratocumulus, *Monthly Weather Rev., 128,* 229-243, 2000.

Kiehl, J.T., T.L. Schneider, P.J. Rasch, M.C. Barth, and J.Wong, Radiative forcing due to sulfate aerosols from simulations with the National Center for Atmospheric Research community climate model, Version 3, *J. Geophys. Res., 105,* 1441-1457, 2000.

Laaksonen, A., T. Vesala, M. Kulmala, P.M. Winkler, and P.E. Wagner, On cloud modelling and the mass accommodation coefficient of water, *Atmos. Chem. Phys. Discuss., 4.,* 7281-7290, 2004.

Lohmann, U., and J. Feichter, Impact of sulfate aerosols on albedo and lifetime of clouds: a sensitivity study with the ECHAM4 GCM, *J. Geophys. Res., 102,* 13685-13700, 1997.

Lohmann, U., J. Feichter, J.E. Penner, and R. Leaitch, Indirect effect of sulfate and carbonaceous aerosols: A mechanistic treatment, *J. Geophys. Res., 105,* 12193-12206, 2000.

Lohmann, U., J. Feichter, C.C. Chuang, and J.E. Penner, Prediction of the number of cloud droplets in the ECHAM GCM, *J. Geophys. Res., 104,* 9169-9198, 1999.

Lohmann, U., J. Feichter, J.E. Penner, and W.R. Leaitch, Indirect effect of sulfate and carbonaceous aerosols: A mechanistic treatment, *J. Geophys. Res., 105,* 12193-12206, 2000.

Ming, Y., and L.M. Russell, Predicted hygroscopic growth of sea salt aerosol, *J. Geophys. Res., 106,* 28259-28274, 2001.

Ming, Y., and L.M. Russell, Organic aerosol effects on fog droplet spectra, *J. Geophys. Res., 109,* 10.1029/2003JD004427, 2004.

Ming, Y., V. Ramaswamy, P.A. Ginoux, L.H. Horowitz, and L.M. Russell, GFDL GCM simulations of the indirect radiative effects of anthropogenic aerosols, *J. Geophys. Res.,* submitted, 2004a.

Ming, Y., V. Ramaswamy, L.J. Donner, and V.T.J. Phillips, A robust parameterization of cloud droplet activation, *J. Atmos. Sci.,* submitted, 2004b.

Moorthi, S., and M.J. Suarez, Relaxed Arakawa-Schubert: a parameterization of moist convection for general circulation models, *Mon. Wea. Rev., 120,* 978-1002.

O'Dowd, C.D., M.H. Smith, and I.W. Consterdine, Marine aerosol, sea-salt, and the marine sulfur cycle: A short review, *Atmos. Environ., 31,* 73-80, 1997.

Pruppacher, H.R., and J.D. Klett, *Microphysics of Clouds and Precipitation*, Kluwer Academic Publishers, 1997.

Ramanathan, V., P.J. Crutzen, J.T. Kiehl, and D. Rosenfeld, *Aerosols, climate, and the hydrological cycle, 294,* 2119-2124, 2001.

Ramaswamy, V., and coauthors, Radiative Forcing of Climate Change, in Climate Change 2001, The Scientific Basis, Contribution of Working Group I to the Third

Assessment Report of the Intergovernmental Panel on Climate Change (IPCC), edited by J. T. Houghton *et al.*, pp. 349-416, Cambridge Univ. Press, UK, 2001.

Rotstayn, L.D., A physically based scheme for the treatment of stratiform clouds and precipitation in large-scale models. 1: Description and evaluation of microphysical processes, *Quart. J. Roy. Met. Soc., 123,* 1227-1282, 1997.

Rotstayn, L.D., B. Ryan, and J. Katzfey, A scheme for calculation of the liquid fraction in mixed-phase clouds in large-scale models, *Mon. Wea. Rev., 128,* 1070-1088, 2000.

Rotstayn, L.D., Indirect forcing by anthropogenic aerosols: a global climate model calculation of the effective-radius and cloud-lifetime effects, *J. Geophys. Res., 104,* 9369-9380, 1999.

Russell, L.M., K.J. Noone, R.J. Ferek, R.A. Pockalny, R.C. Flagan, and J.H. Seinfeld, Combustion organic aerosol as cloud condensation nuclei in ship tracks, *J. Atmos. Sci., 57,* 2591-2606, 2000.

Tie, X., G. Brasseur, L. Emmons, L. Horowitz, and D. Kinnison, Effects of aerosols on tropospheric oxidants: A global model study, *J. Geophys. Res., 106,* 22931-22964, 2001.

Tie, X., S. Madronich, S. Walters, D.P. Edwards, P. Ginoux, N. Mahowald, R. Zhang, C. Lou, and G. Brasseur, Assessment of the global impact of aerosols on tropospheric oxidants, *J. Geophys. Res.,* submitted, 2005.

Tiedtke, M., Representation of clouds in large-scale models, *Mon. Wea. Rev., 212,* 3040-3061, 1993.

Twomey, S., Influence of pollution on the short-wave albedo of clouds, *J. Atmos. Sci., 34,* 1149-1152, 1977.

Whitby, K., The physical characteristics of sulfate aerosols, *Atmos. Environ., 12,* 135-159, 1978.

Yi Ming, Visiting Scientist Program, University Corporation for Atmospheric Research, Geophysical Fluid Dynamics Laboratory, Princeton, NJ 08542. (e-mail: Yi.Ming@noaa.gov); V. Ramaswamy, Geophysical Fluid Dynamics Laboratory, Princeton, NJ 08542. (e-mail: V.Ramaswamy@noaa.gov); Leo J. Donner, Geophysical Fluid Dynamics Laboratory, Princeton, NJ 08542. (e-mail: Leo.J.Donner@noaa.gov); Vaughan T.J. Phillips, Geophysical Fluid Dynamics Laboratory, Princeton, NJ 08542. (e-mail: Vaughan.Phillips@noaa.gov); Stephen A. Klein, Atmospheric Science Division (L-103), Lawrence Livermore National Laboratory, P.O. Box 808, Livermore, CA 94551. (e-mail: klein21@llnl.gov); Paul A. Ginoux, Geophysical Fluid Dynamics Laboratory, Princeton, NJ 08542. (e-mail: Paul.Ginoux@noaa.gov); Larry H. Horowitz, Geophysical Fluid Dynamics Laboratory, Princeton, NJ 08542. (e-mail: Larry.Horowitz@noaa.gov)

Received Date?, 2004; revised Date?, 2004; accepted Date?, 2004.

---

[1] Visiting Scientist Program, University Corporation for Atmospheric Research, Geophysical Fluid Dynamics Laboratory, Princeton, NJ

[2] Geophysical Fluid Dynamics Laboratory, Princeton, NJ

[3] Lawrence Livermore National Laboratory, Livermore, CA

Submitted November, 2004.

Table 1. Mean flux changes due to indirect effects (W m^{-2}), with shortwave components in parentheses.

	Global Annual	January	July	NH	SH	Land	Ocean
BASE	-1.8 (-2.0)	-0.8 (-0.9)	-2.2 (-2.8)	-2.2 (-2.5)	-0.7 (-0.5)	-2.2 (-2.1)	-1.6 (-1.9)
NOOC	-1.1 (-1.5)	-1.1 (-1.2)	-1.5 (-2.1)	-1.6 (-2.4)	-0.3 (-0.2)	-1.5 (-2.4)	-1.0 (-1.2)
Diagnostic	-2.3 (-2.7)	-1.8 (-1.7)	-2.9 (-3.5)	-3.3 (-3.6)	-0.8 (-0.9)	-1.7 (-2.3)	-2.6 (-2.8)

Figure 1. Parcel model-simulated cloud supersaturation as a function of height above cloud base at a constant updraft velocity of 1 m s^{-1}. The solid, dotted and dashed lines correspond to different entrainment rates (0, 1.8×10^{-4} and 1.8×10^{-3} m^{-1}, respectively).

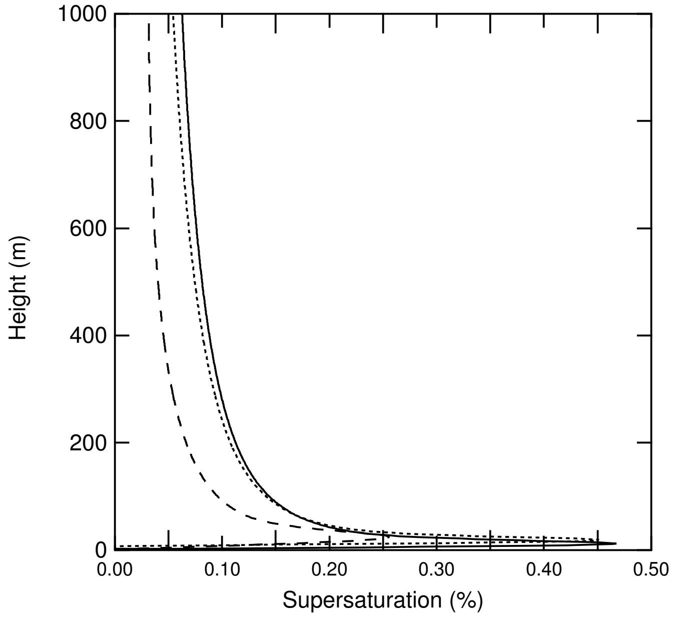

Figure 2. PI and PD column burdens of sulfate, OC and sea-salt (mg m^{-2}) in January and July.

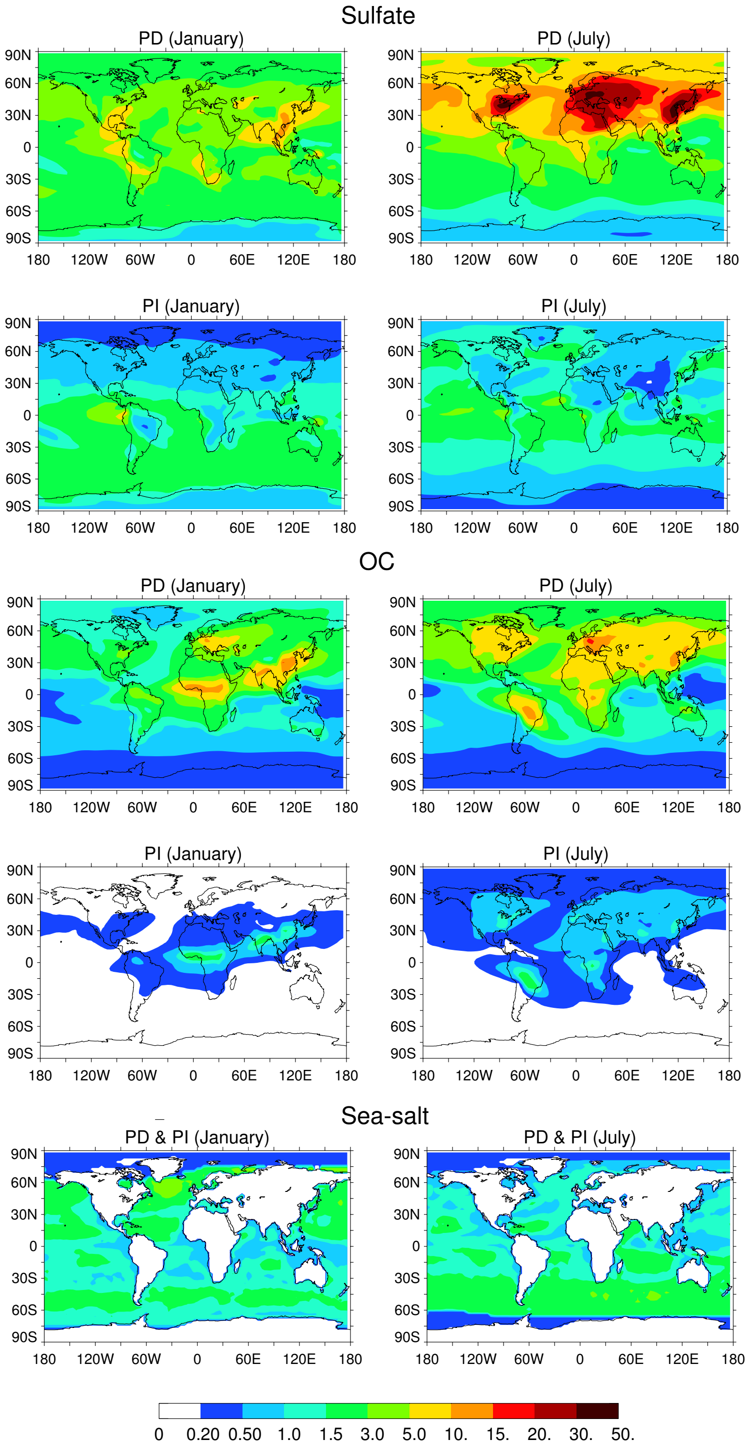
Sulfate
PD (January)
PD (July)
PI (January)
PI (July)
OC
PD (January)
PD (July)
PI (January)
PI (July)
Sea-salt
PD & PI (January)
PD & PI (July)
90N
60N
30N
0
30S
60S
90S
180
120W
60W
0
60E
120E
180
0
0.20
0.50
1.0
1.5
3.0
5.0
10.
15.
20.
30.
50.

Figure 3. Geographical distributions of N_d (cm^{-3}) at 904 mb in January and July predicted with the prognostic cloud scheme (the top panels) and diagnosed from sulfate mass concentrations using BL95 (the bottom panels).

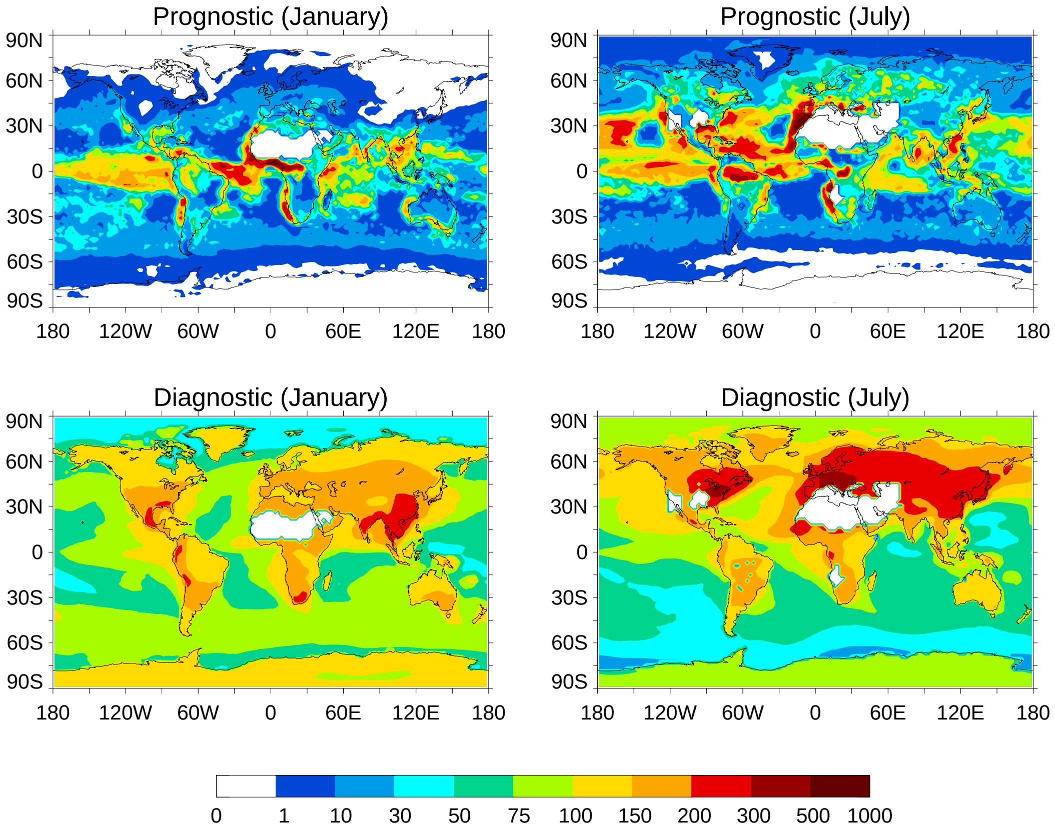
Prognostic (January)
Prognostic (July)
Diagnostic (January)
Diagnostic (July)
90N
60N
30N
0
30S
60S
90S
180
120W
60W
0
60E
120E
180
0
1
10
30
50
75
100
150
200
300
500
1000

Figure 4. Tendencies of sources and sink of n (kg(air)$^{-1}$ s^{-1}) at 904 mb in January and July in the prognostic cloud scheme (the top panels: convective source; the middle panels: large-scale source; the bottom panels: large-scale sinks).

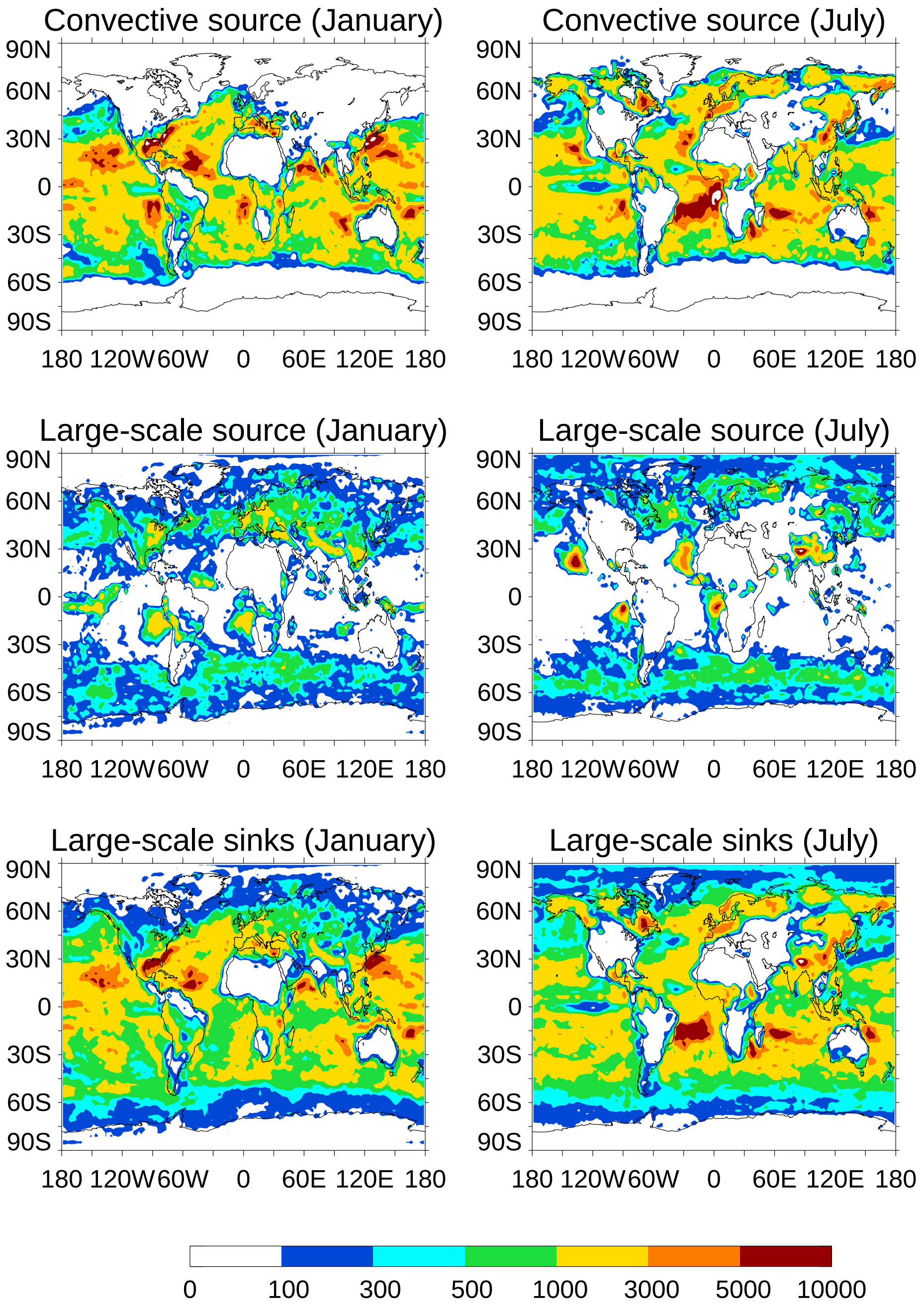
Convective source (January)
Convective source (July)
Large-scale source (January)
Large-scale source (July)
Large-scale sinks (January)
Large-scale sinks (July)
90N
60N
30N
0
30S
60S
90S
180 120W 60W 0 60E 120E 180
0
100
300
500
1000
3000
5000
10000

Figure 5. Vertical distributions of N_d (cm^{-3}) in January and July predicted with the prognostic cloud scheme (the top panels) and diagnosed from sulfate mass concentrations using BL95 (the bottom panels).

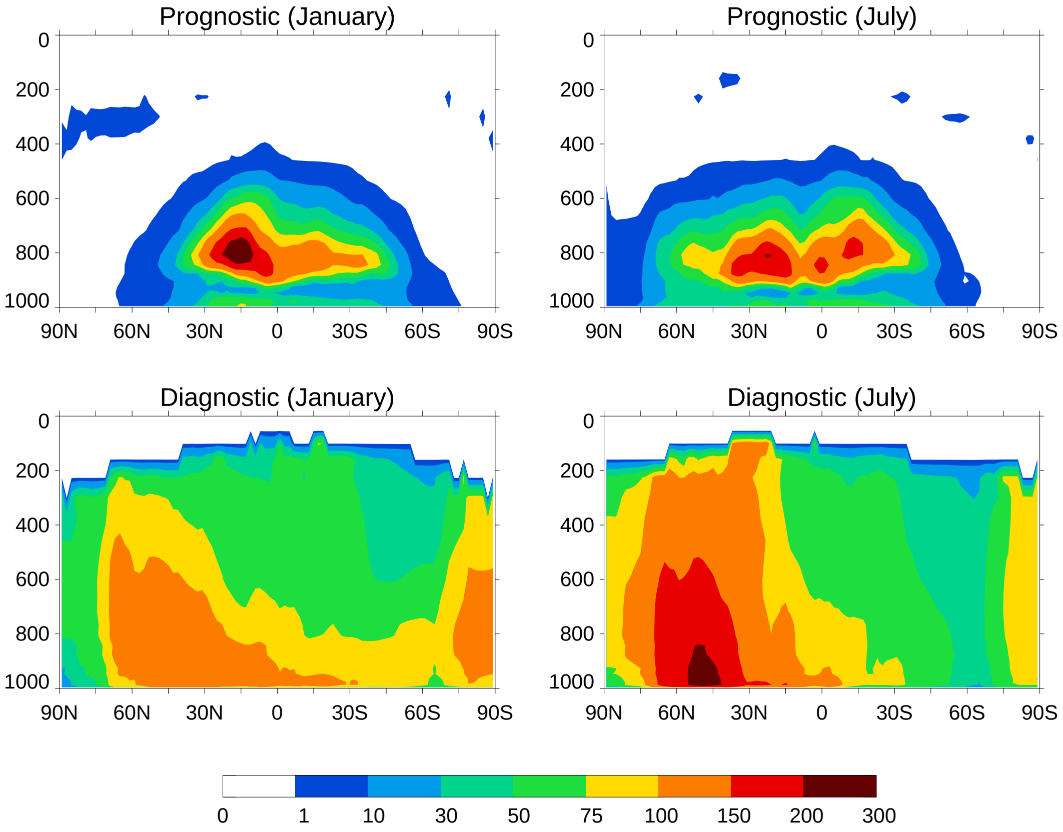

Figure 6. Zonal mean liquid water path over ocean in January (top panel) and July (bottom panel) simulated with prognosed N_d (solid lines) and with diagnosed N_d (dotted lines), and inferred from SSM/I measurements (crosses: *Greenwald et al.* [1995]; circles: *Weng and Grody* [1994]).

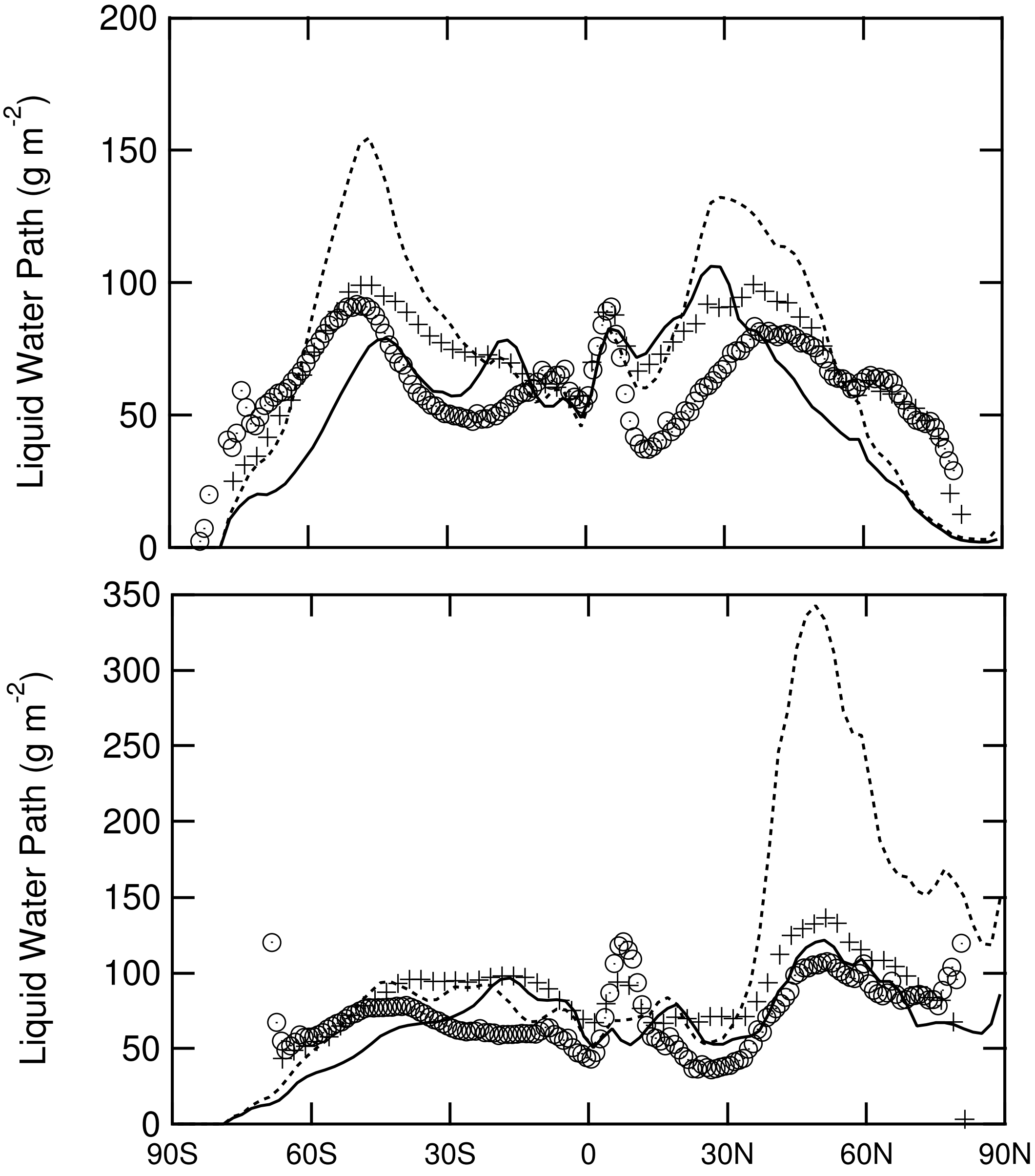

Figure 7. Zonal mean cloud optical depth in January (top panel) and July (bottom panel) simulated with prognosed N_d (solid lines) and with diagnosed N_d (dotted lines), and inferred from ISCCP measurements (crosses).

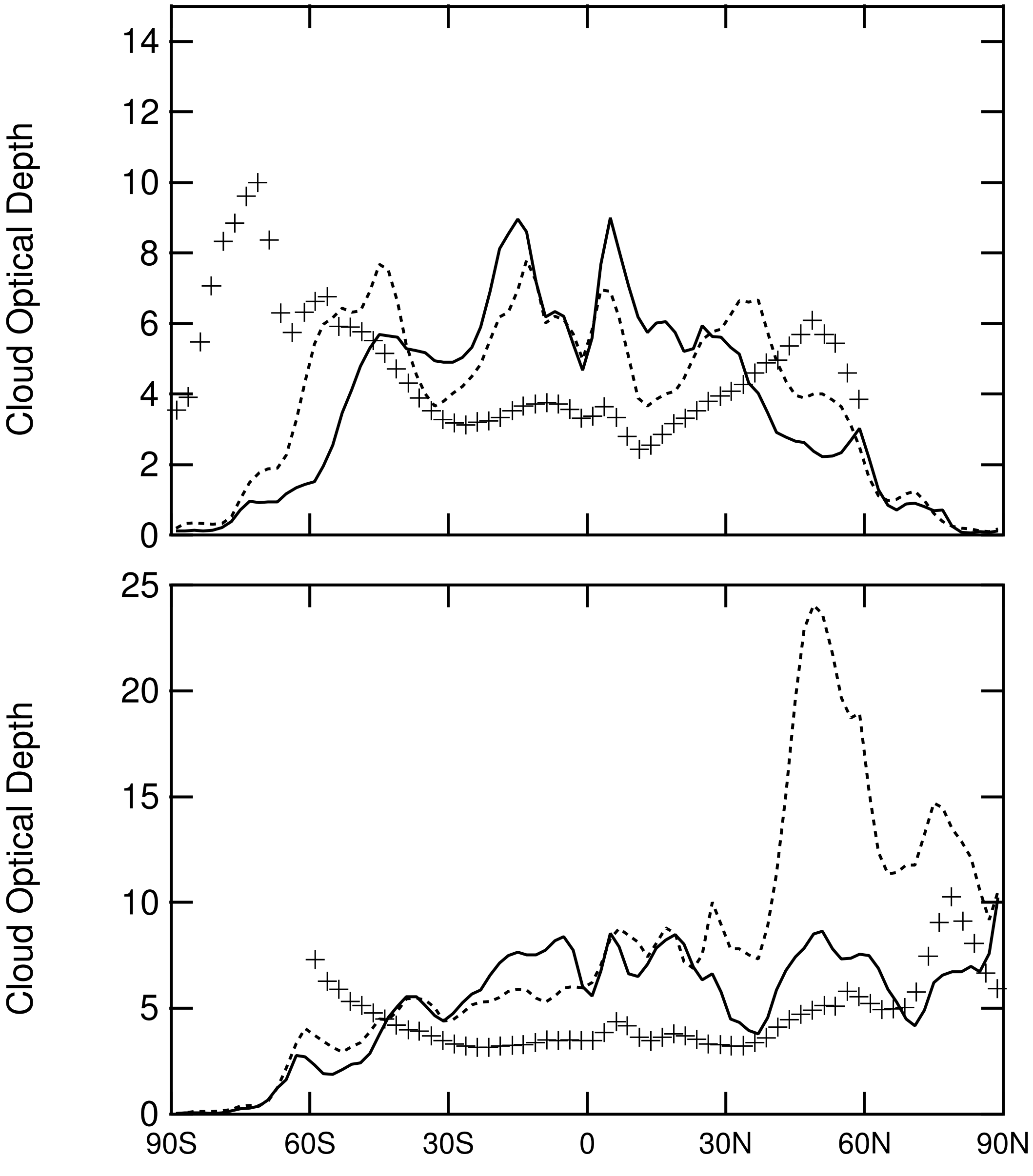

Figure 8. Zonal mean total cloud amount in January (top panel) and July (bottom panel) simulated with prognosed N_d (solid lines) and with diagnosed N_d (dotted lines), and inferred from ISCCP measurements (crosses).

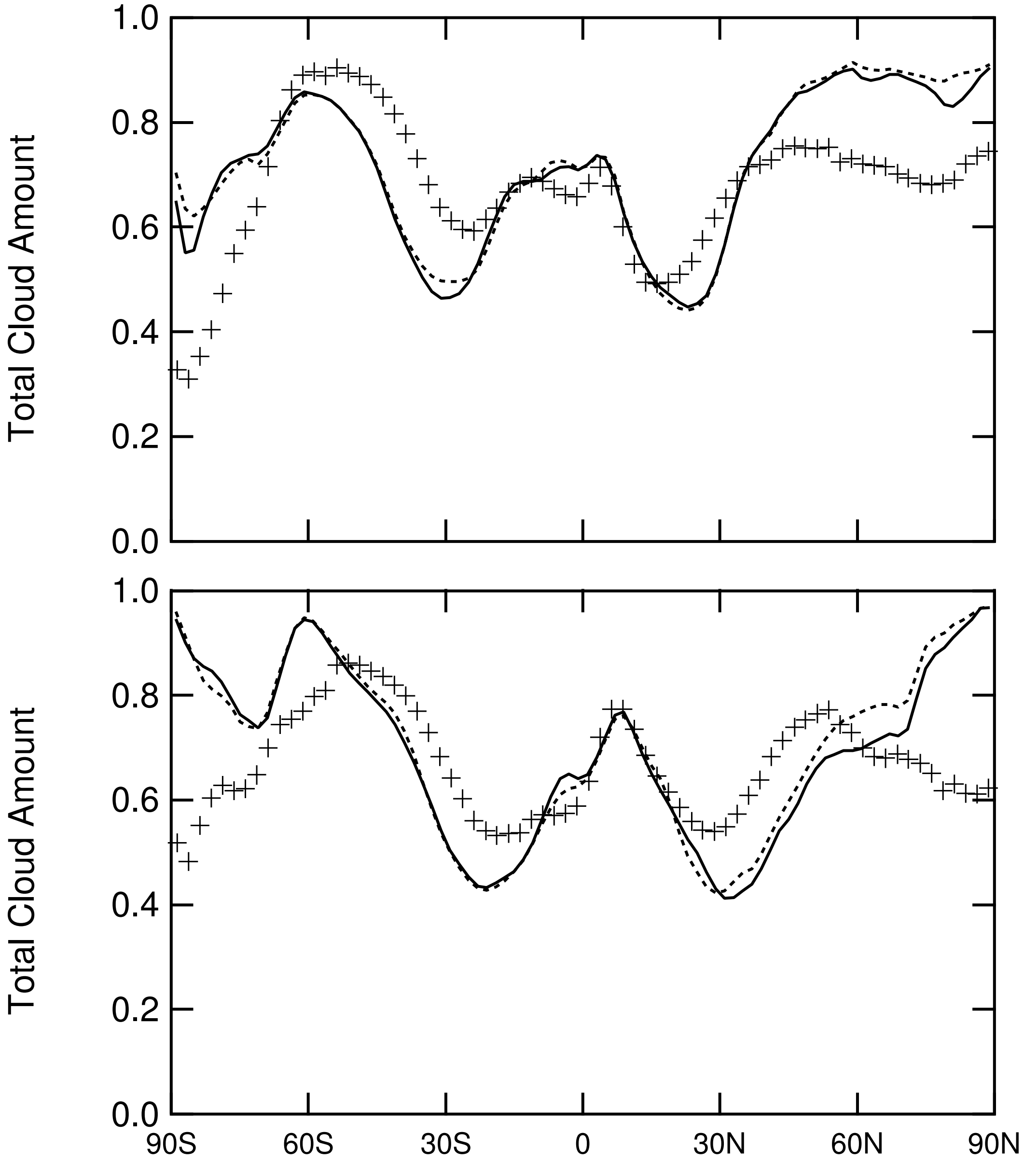

Figure 9. Zonal mean shortwave cloud forcing in January (top panel) and July (bottom panel) simulated with prognosed N_d (solid lines) and with diagnosed N_d (dotted lines), and inferred from ERBE measurements (crosses).

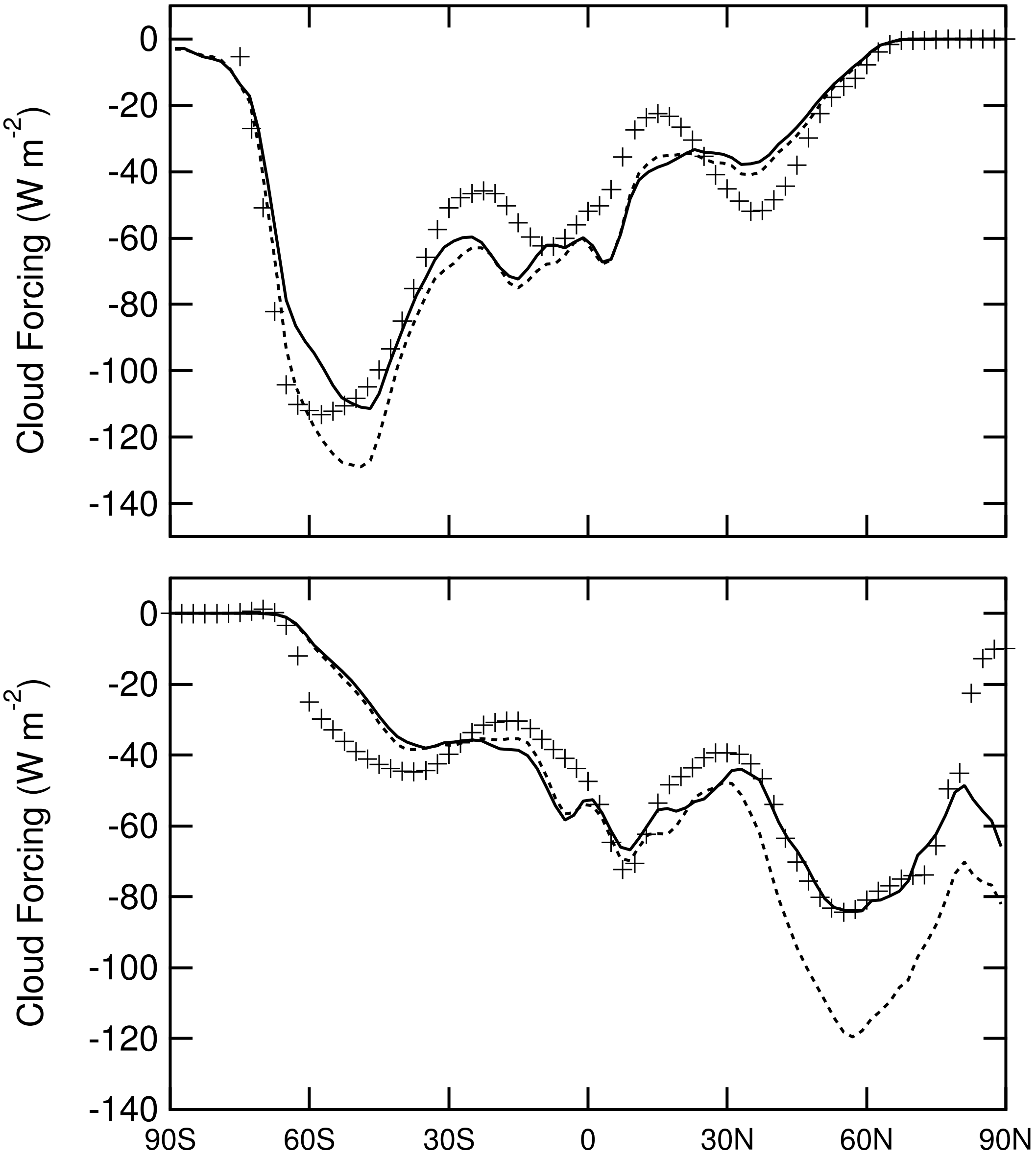

Figure 10. Zonal mean longwave cloud forcing in January (top panel) and July (bottom panel) simulated with prognosed N_d (solid lines) and with diagnosed N_d (dotted lines), and inferred from ERBE measurements (crosses).

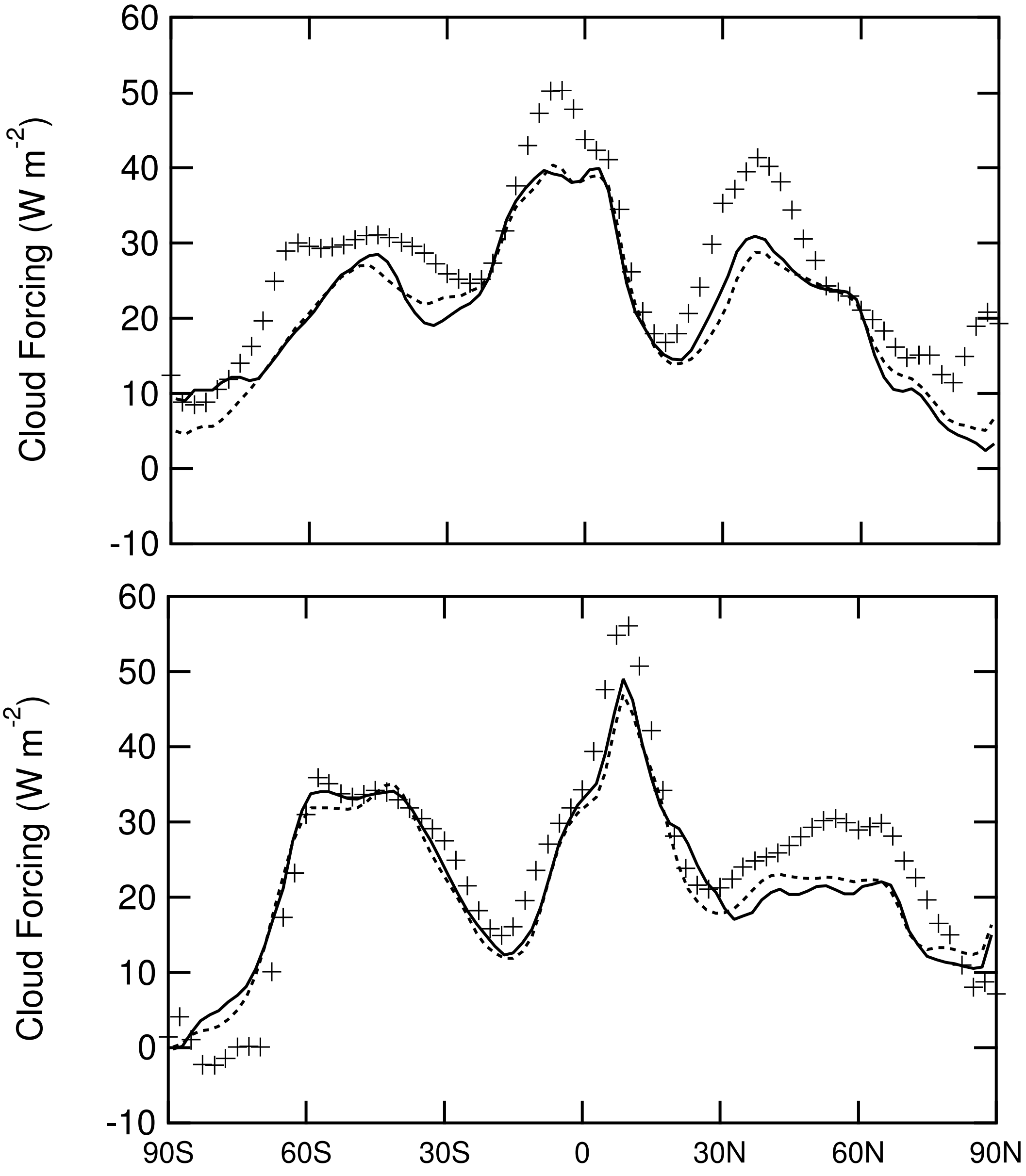

Figure 11. Geographical distribution of flux changes (W m^{-2}) at TOA in BASE.

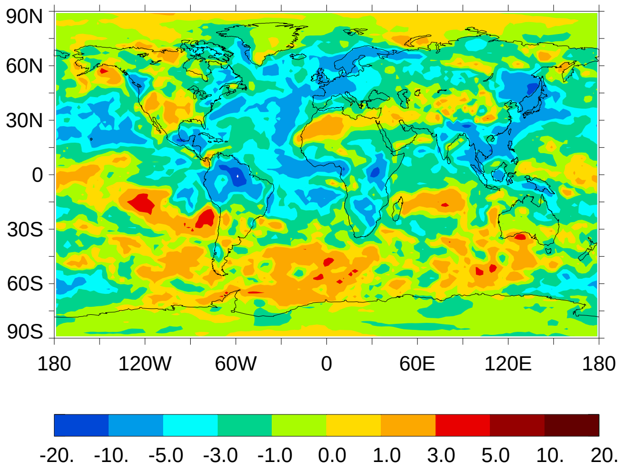
90N
60N
30N
0
30S
60S
90S
180
120W
60W
0
60E
120E
180
-20.
-10.
-5.0
-3.0
-1.0
0.0
1.0
3.0
5.0
10.
20.

Figure 12. Geographical distributions of SW (the top panel) and LW (the bottom panel) flux changes (W m^{-2}) at TOA in BASE.

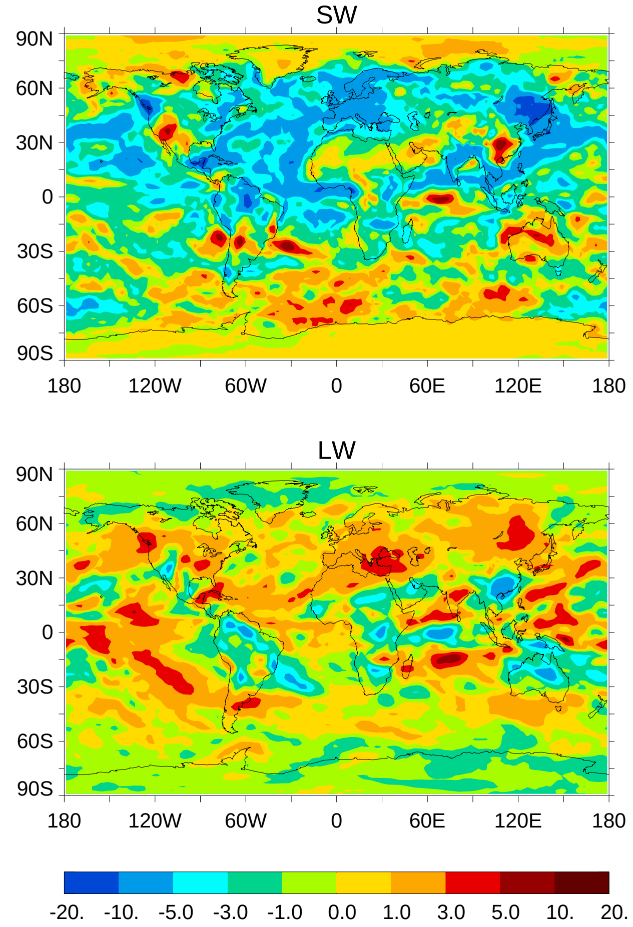
SW
90N
60N
30N
0
30S
60S
90S
180
120W
60W
0
60E
120E
180
LW
90N
60N
30N
0
30S
60S
90S
180
120W
60W
0
60E
120E
180
-20.
-10.
-5.0
-3.0
-1.0
0.0
1.0
3.0
5.0
10.
20.

Figure 13. Geographical distributions of changes in LWP (mg m^{-2}) in BASE (the top panel) and using diagnosed N_d (the bottom panel).

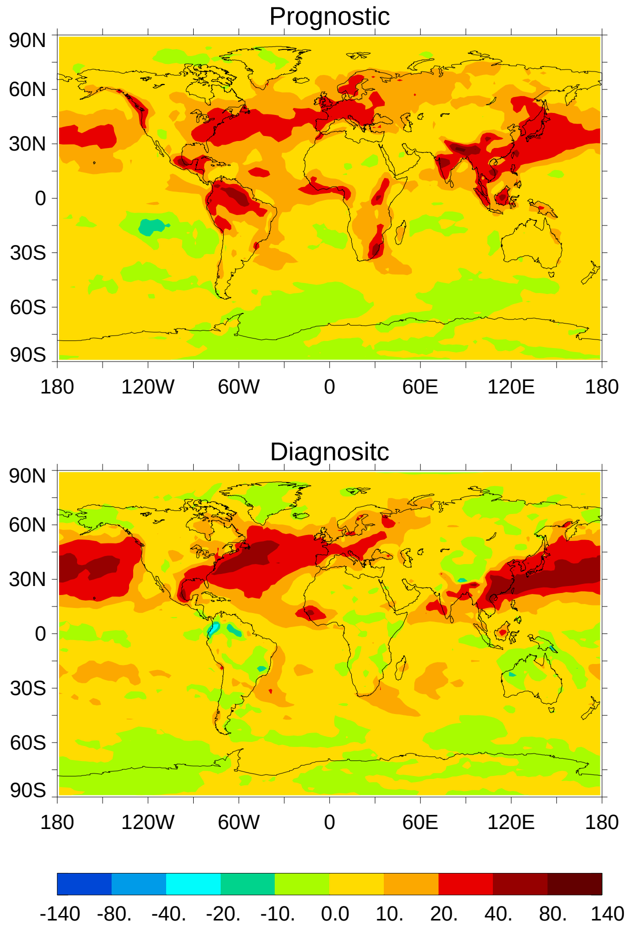

Prognostic

Diagnositc

90N
60N
30N
0
30S
60S
90S
180
120W
60W
0
60E
120E
180
-140
-80.
-40.
-20.
-10.
0.0
10.
20.
40.
80.
140

Figure 14. Same as Fig. 11 except for NOOC (the top panel). The results with diagnosed N_d (the bottom panel) are for comparison.

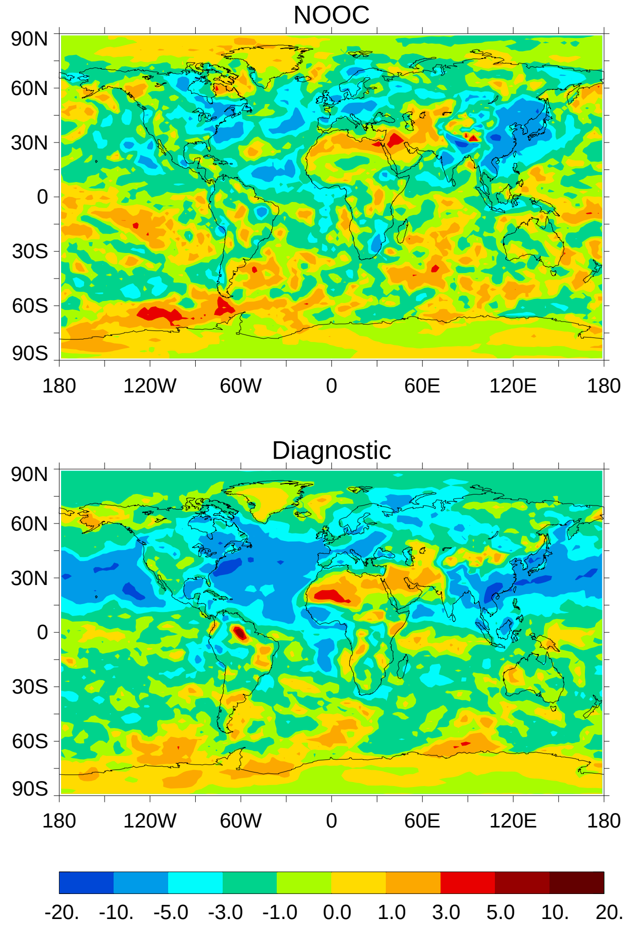
NOOC
90N
60N
30N
0
30S
60S
90S
180
120W
60W
0
60E
120E
180
Diagnostic
90N
60N
30N
0
30S
60S
90S
180
120W
60W
0
60E
120E
180
-20.
-10.
-5.0
-3.0
-1.0
0.0
1.0
3.0
5.0
10.
20.

Figure 15. Annual zonal mean flux changes (W m^{-2}) in BASE (the thick solid line) and in NOOC (the thick dotted line). The model's natural variations are characterized by the standard deviations (the error bars).

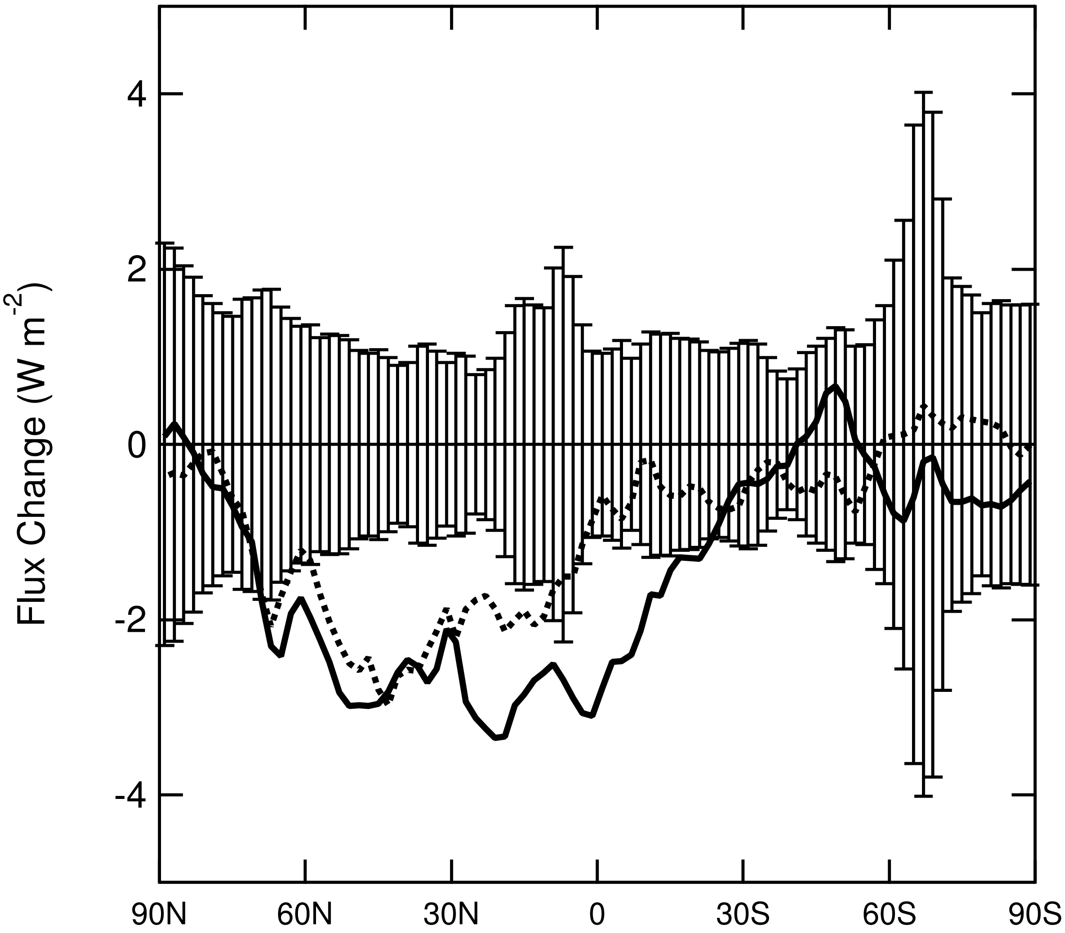

Figure 16. Dependence of CCN activation on updraft velocity. The crosses represent parcel model results, from which the solid straight line is fitted (correlation coefficient $R^2 = 0.996$).

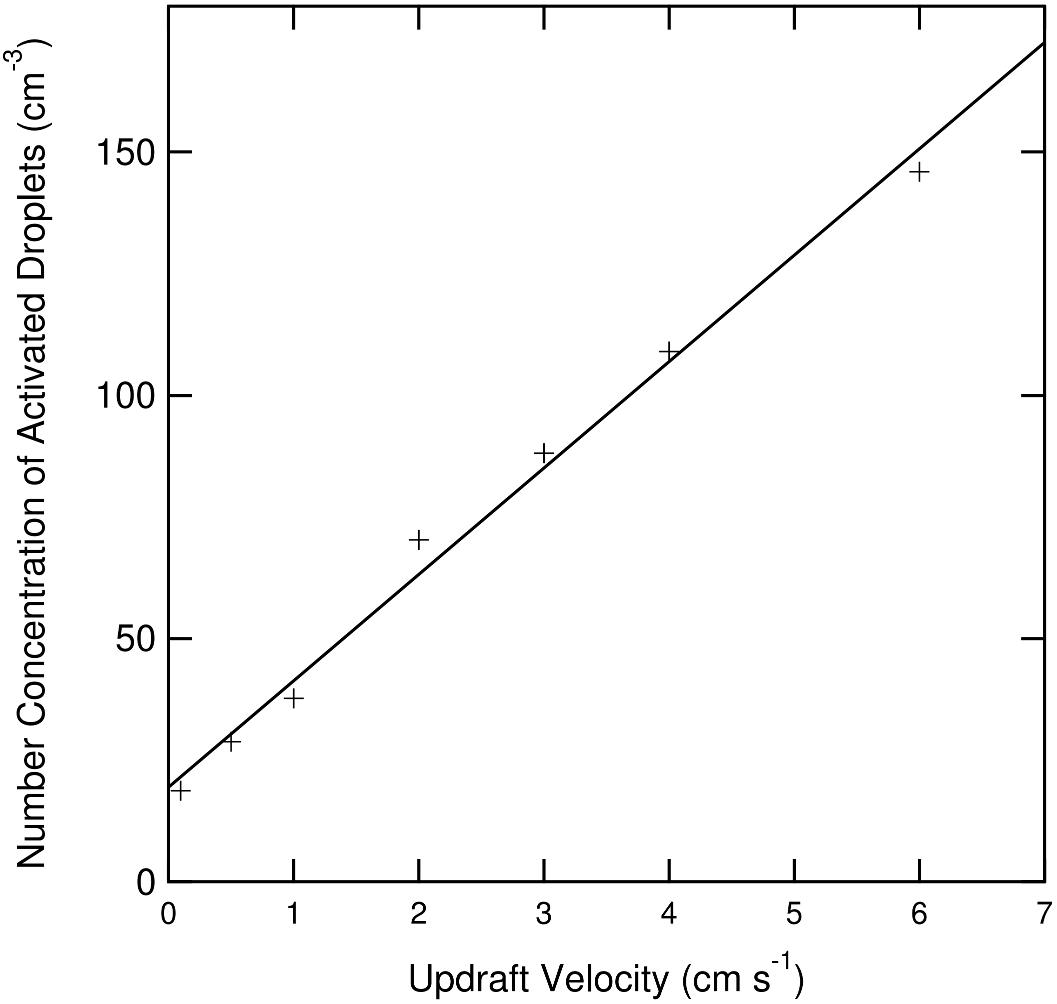

Figure 17. Scatter plot of prognosed N_d versus sulfate concentrations over land (top panel) and over ocean (bottom panel) of 20°N to 60°N. In each panel, the dotted line represents the mean values, which are bounded by the dashed lines with one standard deviation. The solid line represents the empirical relationship of BL95.

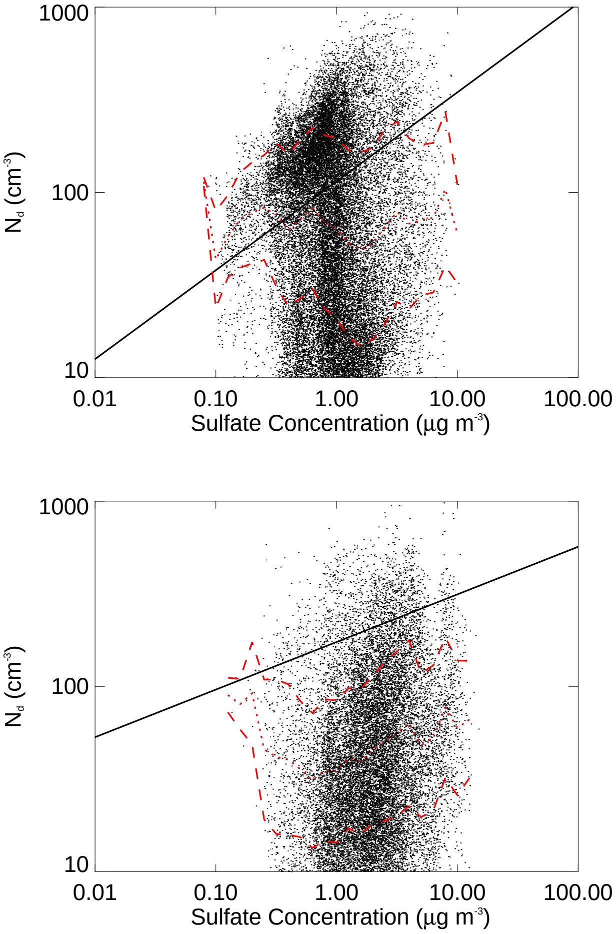

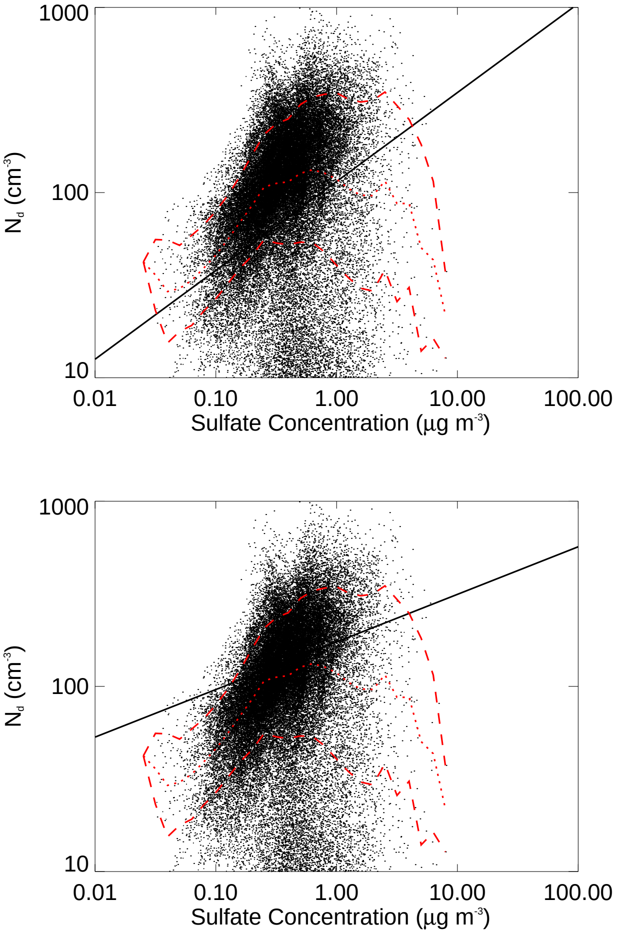Figure 18. Same as Fig. 17 except for 20°S to 20°N.